Nuclear Engineering and Technology 58 (2026) 104548

Contents lists available at ScienceDirect

Nuclear Engineering and Technology

journal homepage: www.elsevier.com/locate/net

Original Article

Integration scenario of a distributed Traveling Wave Antenna in European DEMO

Amro Bader [a,*], Francisco A. Hernández [b], Riccardo Ragona [c], Guangming Zhou [b]

[a] Max–Planck-Institut für Plasmaphysik, Boltzmannstrasse 2, Garching b. München, 85748, Germany
[b] Karlsruhe Institute of Technology, Eggenstein-Leopoldshafen, Karlsruhe, 76344, Germany
[c] Technical University of Denmark, Department of Physics, Lyngby, 2800, Denmark

ARTICLE INFO

Keywords:
Traveling Wave Antenna
DEMO
Remote handling compatibility
Breeding blanket
Tritium breeding ratio

ABSTRACT

A preliminary engineering feasibility study of the integration of a Traveling Wave Antenna (TWA) in European DEMO is presented. Unlike conventional ICRF antennas in vacuum vessel ports, the TWA is embedded in blanket segments, avoiding the dimensional constraints imposed by such ports. Thus, a substantial increase in the antenna surface area can be achieved, thereby reducing the surface power density. This is particularly important for larger machines like DEMO, where higher power levels are needed for plasma heating. This work presents initial assessments of how this integration affects tritium breeding, thermo–hydraulic performance, and remote-handling compatibility of the blanket. The analysis indicated a reduction in the blanket's tritium breeding ratio by only 2%. Thermo–hydraulic analysis indicated that the maximum temperatures obtained remain below 550°C for a Eurofer based antenna, and the pressure drop in the antenna cooling circuit generally remains below 5 kPa. The structural checks of the antenna straps indicated compliance with the RCC-MRx design rules for monotonic damage modes under standard operating loads. The compatibility of the antenna with remote handling of the blanket segment was assessed and no fundamental incompatibility was identified for the present configuration. This early screening-level study aims to pave the way for further engineering refinement of the integration of TWA in DEMO.

1. Introduction

The Ion Cyclotron Range of Frequencies (ICRF) is among the candidate plasma-heating systems for larger machines like European DEMO (EU-DEMO, or simply DEMO, hereafter). However, the required heating powers of several tens of megawatts in such devices place stringent demands on antenna performance and integration. Conventional in-port antenna concepts, including the toroidally-arranged halves configuration [1], remain constrained by the limited dimensions of the vacuum vessel (VV) ports, as indicated in Fig. 1. This restriction limits the available radiating surface area, leading to elevated power densities on the antenna surface and potentially compromising long-term reliability.

The Traveling Wave Antenna (TWA) concept has been proposed to overcome these limitations by embedding the antenna within the breeding blanket, where a significantly larger surface area is available for power coupling when compared to vacuum vessel ports. This approach enables the delivery of 50 MW at lower surface power densities because the antenna surface can be substantially increased inside the breeding blanket. One critical design driver is the voltage stand-off limitations on antenna transmission lines (TL). For a 3-inch (76 mm) coaxial line with characteristic impedance $Z_0 = 50\ \Omega$, the TL voltage should not exceed 30 kV, which corresponds to a maximum power of 9 MW per line.

Extensive progress has already been achieved in the plasma physics aspects of the TWA [2–6], including optimizing the number of straps, inter-strap distances, directivity, and load matching. However, detailed studies of how such an antenna can be physically accommodated within DEMO – while still respecting thermo–hydraulic, tritium breeding, and remote handling constraints – remain limited.

In this work, we present an engineering integration scenario for the TWA in DEMO, including remote handling and tritium breeding ratio assessment, thermo–hydraulic analysis, and structural integrity considerations (see Fig. 1).

2. TWA configuration

2.1. The antenna

The Traveling Wave Antenna (TWA) consists of toroidally distributed metallic launchers ("straps") housed within recesses in the

* Corresponding author.
E-mail address: amro.bader@postgrad.manchester.ac.uk (A. Bader).

https://doi.org/10.1016/j.net.2026.104548
Received 16 April 2026; Received in revised form 6 June 2026; Accepted 5 July 2026
Available online 11 July 2026

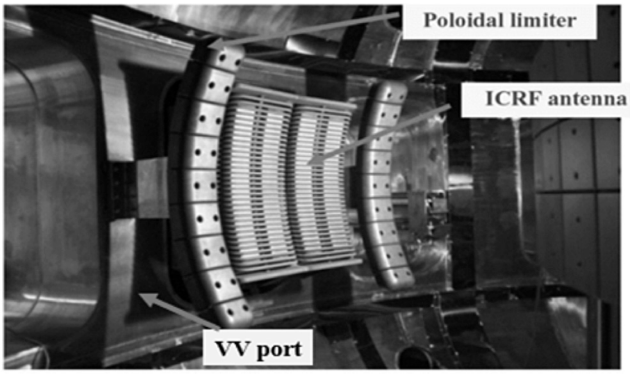

Fig. 1. Standard ICRF antenna located in a vacuum vessel port with various parts labeled.
Source: Modified from Fig. 12 in [7].

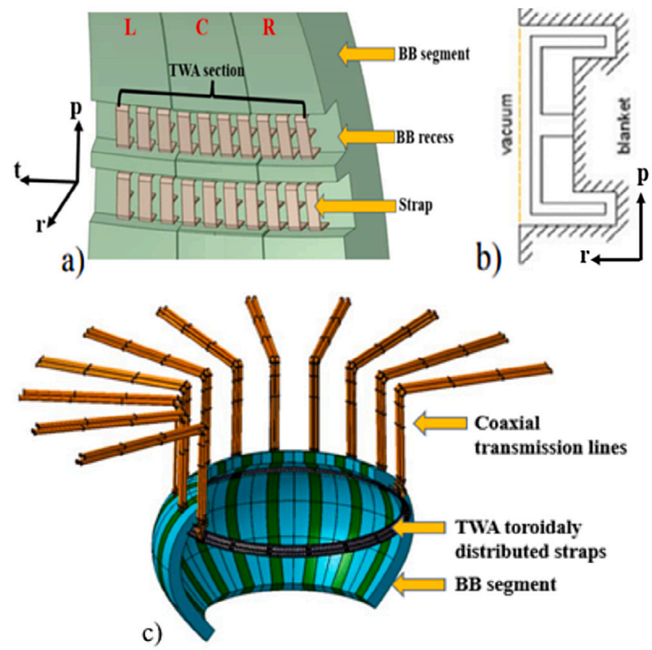

Fig. 2. (a) TWA double section of 20 straps covering three blanket segments with letters L, C, and R referring to the left, center, and right segments, (b) sketch of a T-shaped strap attached to the blanket, and (c) view of 16 TWA double sections covering the full blanket circumference (ring configuration), with transmission lines.

breeding blanket (BB) segments. The toroidal extension of the antenna can span the entire circumference of the machine, forming a "ring" strap array or a fraction of it (from 1 to 16 TWA sections in DEMO, which comprises 16 BB sectors). The fundamental building blocks of the TWA are the TWA sections, defined as a group of straps that cover three toroidal BB segments. For the present study, each TWA section consists of two sets of 10 straps on top of each other, as Fig. 2a indicates.

DEMO has 16 vacuum vessel (VV) sectors [8, page 9], each containing three outboard (OB) and two inboard (IB) segments. Consequently, a TWA section covers one outboard BB sector (i.e. 1/16 of the machine circumference), while a ring array consists of 16 sections, covering all BB sectors (Fig. 2a, c).

The straps are assumed to be made of Eurofer steel, consistent with the structural material of BB, and could be protected by a 1 to 2 mm tungsten armor layer similar to the First Wall (FW), to reduce sputtering. The straps are mechanically attached to the BB via a central connection (Fig. 2(b) and have the following dimensions: 500 mm in the poloidal direction, 225 mm in the radial direction, and 200 mm in the toroidal direction.

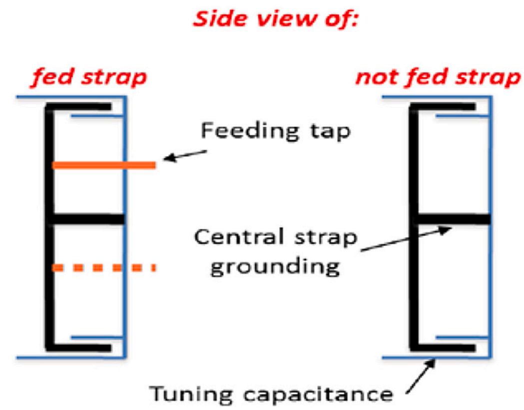

Fig. 3. Schematic of an actively-fed strap (left) and a passive strap. Continuous orange line represents a TL, while the dashed line below it reflects the possibility to feed a strap using one or two TLs. This work assumes two feeding lines per strap.

2.2. *Antenna feeding*

Radio Frequency power is delivered to the TWA sections using the resonant ring feeding scheme [9], where only the first strap in the section is actively fed using two transmission lines (TLs). The remaining straps receive power passively via inductive coupling from the actively-fed strap. The remaining, non-radiated power is recirculated back into the resonant ring using two TLs that are connected to the last strap in the section. Straps directly connected to a TL are referred to as active straps, while all other straps are passive. Each active strap is connected to two coaxial TLs, each with an outer diameter of 3-inch (76 mm). With the configuration presented in (Fig. 2(a), eight TLs are required: four for actively feeding power, and four to extract the non-radiated power. The TLs access the vacuum vessel through the vertical port (VP) above the central outboard blanket segment (COBS). It is possible to feed using a single TL only (that is, four TLs per sector); however, this requires larger line diameters and is more challenging for blanket integration. Fig. 3 shows a schematic of the strap power-feeding arrangement.

3. Integration in DEMO

The TWA integration in DEMO will have interfaces mainly with the breeding blanket and the vacuum vessel's vertical ports environment. A qualitative description of the integration requirements and challenges was summarized in [10]. In the following and subsequent sections, a description of the blanket architecture is given before a detailed integration scenario with the blanket is proposed.

3.1. *Integration guidelines*

Integrating the antenna in the blanket is guided by a few considerations, mainly:

- it should be compatible with the remote handling procedures of the blanket, such that breeding blanket segments are fully maintainable without extra complexity,
- it should not affect the tritium breeding ratio of the blanket (i.e., a TBR $\geq$ 1.15 should be at least achieved according to [11] after the antenna is integrated into the blanket),

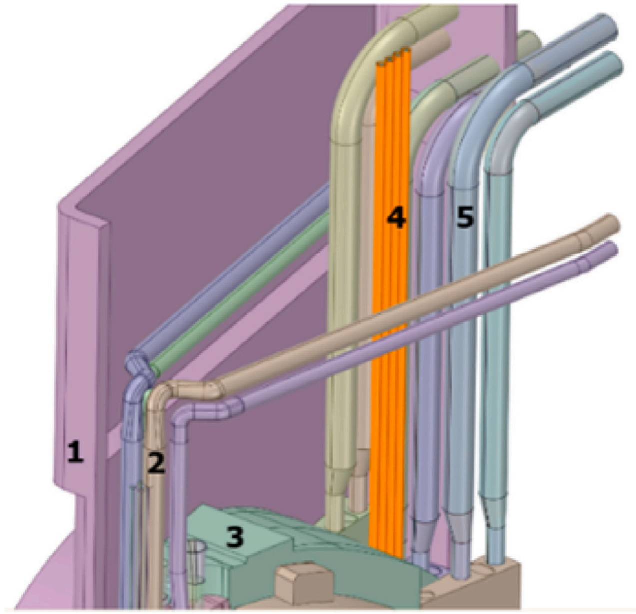

Fig. 4. TLs in the upper port (orange, number 4). Other components are the vacuum vessel (1), blanket coolant pipes (2 and 5), and a port plug (3).

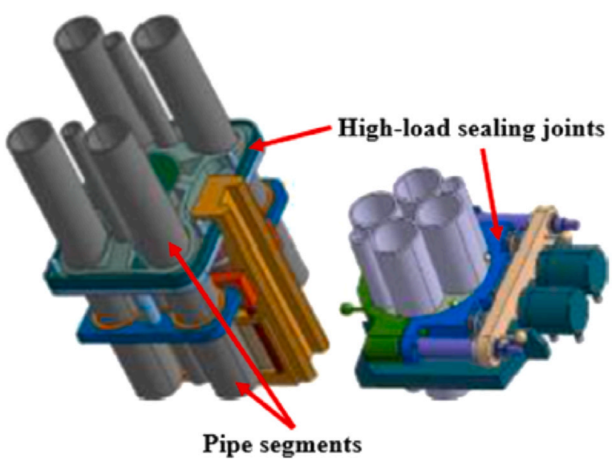

Fig. 5. Multiple-pipe mechanical joint for DEMO blanket coolant pipes. *Source:* (modified from Fig. 24 in [12])

- the Eurofer-made antenna (straps and TLs) should be maintained within an acceptable operating temperature range, i.e. 300 °C < T < 550 °C with a coolant pressure drop of the order of 5 kPa, similar to the breeding pins (as described in more detail in Section 3.3.1),
- the antenna should demonstrate structural integrity at least under the structural loading conditions associated with normal operation.

Each of these points is technically supported, expanded, and investigated in the following sections.

3.2. Remote handling compatibility assessment

3.2.1. Straps

Remote handling (RH) of the blanket segment follows an established procedure [12, pages 4, 5, 6], which is to insert a remotely controlled manipulator that grips the segment and pulls it vertically through the top port. With three blanket segments per top port, the process is performed sequentially, where each segment is lifted independently from the others. This is possible because blanket segments are not inter-connected with each other. The antenna straps – as presented in Fig. 2 – are also not inter-connected, although with a caveat: there could eventually be a need to install a rear structure behind the straps, which traverses multiple blanket segments, for the returning RF currents according to [6,13]. If adopted, this could add a layer of complexity to the RH. Solutions could be developed if needed, but the present antenna configuration does not appear to conflict with RH requirements. Additionally, the RH manipulator is subject to a maximum allowable payload. The integrated antenna subtracts from the blanket volume, and straps themselves are hollow, with volume largely filled by coolant, and therefore no violation of the maximum allowable manipulator load is expected. We conclude that the straps do not appear to jeopardize the RH of the blanket segments, with reference to their configuration as reported in Fig. 2.

Table 1
Radiative cooling model parameters and result.

Boundary conditions/result	Value	Unit
Inlet pipe temperature	300	°C
Outlet pipe temperature	520	°C
Vacuum vessel temperature	200	°C
Emissivity	0.25	NA
View factor	surface-to-surface	NA
Max. TL temperature	400	°C

3.2.2. Transmission lines

The TLs are made of separate segments that are mechanically connected. The length of the segment can vary according to the need. They are much lighter than the blanket segments and can be easily manipulated with RH tools. Fig. 4 shows the TLs (orange) in the top port environment. The TLs occupy a visibly smaller volume in the top port compared to the blanket coolant pipes (all non-orange pipes). Because their geometry is cylindrical, similar to that of blanket coolant pipes, they could likely be handled using existing RH technology.

3.2.3. Transmission lines inter-connection

During maintenance, blanket coolant pipes are cut and re-welded using an in-bore laser welding tool [12, page 13]. This approach is not suitable for the coaxial TLs as a result of the obstruction caused by the inner conductor, which prevents tool access. Consequently, TLs cannot be cut and re-welded in the same manner as blanket pipes, and standard flange-type connections should be considered. One connection method already developed for EU DEMO is the multi-tube mechanical joint [12, page 13], which achieves sealing by applying extremely high loads (on the order of several MN) to press the tube segments together. This concept, illustrated in Fig. 5, is compatible with a commercially available TL diameter range, including DN75. Although such high sealing forces are essential for helium-tight blanket pipe connections, they may not be required for antenna TLs if they can be passively cooled (i.e., no helium flow is required). To assess this, in ANSYS a finite element model (FEM) was developed based on the geometry shown in Fig. 4, to evaluate the feasibility of passive radiative cooling of the TLs. The simulation parameters and results are summarized in Table 1. The primary thermal loads considered were radiative heat transfer from the surrounding environment. Additional heating from RF power dissipation was not included, as these loads are intermittent – occurring mainly during plasma ramp-up or conditioning – and are not expected to be design-driving. Once the RF losses are quantified, the simulations can be refined accordingly. Fig. 6 indicates the resulting TL temperatures, which vary roughly between 350 and 400 °C in the TLs. This result indicates that passive radiative cooling is feasible for the TLs, which greatly simplifies their integration in the top port region.

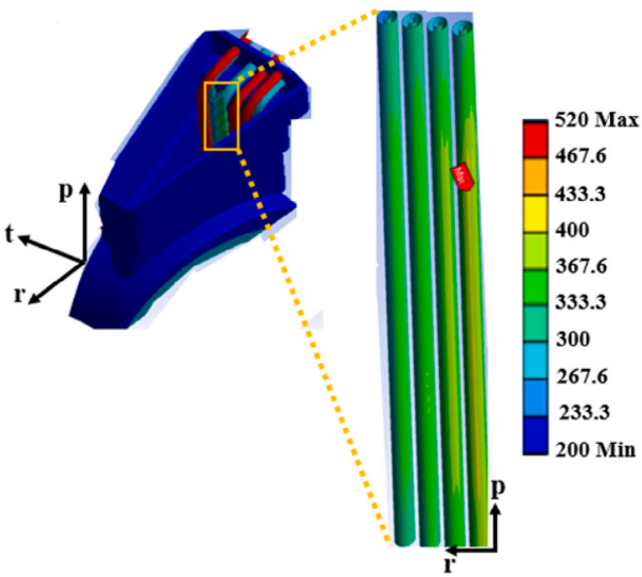

Fig. 6. Temperatures distribution on the transmission lines in the top port region with radiative passive cooling.

Thus, the multiple-tube joint could be used to mechanically connect various TL segments using a relaxed version that does not require massive sealing forces since the TLs are passively cooled. It follows that maximizing the length of the TL segments in the top port area will reduce the number of mechanical joints needed: assuming reasonably 4 to 5 TL segments in the top port, 2 to 3 mechanical joints shall be required. The time to engage and release these joints should be minimal compared to standard flange connections.

This section concludes that the antenna and TLs – in their current configuration – do not jeopardize the RH of the blanket segments. However, we should clarify that the above assessment was made assuming that the antenna does not add any physical connection between blanket modules. Some Radio Frequency considerations could still eventually dictate the need to install one metallic box behind the antenna that could span three blanket segments in the toroidal direction [13]. If eventually adopted, an updated RH assessment should be made. Therefore, the present analysis does not provide fully resolved RH compatibility for all design variants; it only demonstrates compatibility for the current assumed configuration.

3.3. Tritium breeding

Another key factor to assess before detailed antenna integration is the impact of the antenna on the blanket's tritium breeding ratio (TBR), which determines whether sufficient tritium can be bred for fuel self-sufficiency. In this section, we performed a nuclear analysis using Monte Carlo N-Particle Transport 5 (MCNP) for neutron reactions and demonstrated that the TBR is reduced by 2% following antenna integration. The analysis steps are explained below.

3.3.1. Reference blanket concept

Rationale behind blanket selection: Fig. 7 presents the reference breeding blanket concept (BB) considered for antenna integration. The selected option is the Helium-Cooled Pebble Bed (HCPB) blanket [14–16], in which lithium-based ceramic pebbles serve as breeding material and helium is used to cool and purge tritium. The alternative BB concept considered for DEMO is the water-cooled lithium lead (WCLL) blanket [17]. The HCPB was chosen as the reference due to its resemblance at the breeding unit level (pins, shown in Fig. 7) to the TL geometry.

As shown in Fig. 7, the breeder pebbles (the Gray volume referred to as ACB — Advanced Ceramic Pebbles in Fig. 7) are contained in cylindrical pins (∅ = 68 mm) housed within larger pressure tubes (∅ = 82 mm). The cylindrical form and dimensions of the pin allow it to be replaced directly with a TL (∅ ≈ 76 mm), which will be housed inside the pressure tube and consequently make integration simpler. Future work may also explore compatibility with the WCLL concept.

Blanket build-up and relevant dimensions: The HCPB employs Advanced Ceramic Breeder (ACB) pebbles, a mixture Li_4SiO_4 / Li_2TiO_3 and uses beryllide ($Be_{12}Ti$) as a neutron multiplier to ensure the availability of surplus neutrons. The structure is fabricated from Eurofer, a reduced-activation ferritic–martensitic steel. The blanket consists of cylindrical pins aligned radially with a pitch of 125 mm. Each pin is a Eurofer tube of 530 mm length, containing breeder pebbles. The hollow interior of the pin acts as a helium inlet, while the annular gap between the pin and the pressure tube forms the outlet channel. The pressure tube (Eurofer, 4 mm-thick, ⌀ = 82 mm) is externally surrounded by neutron multiplier material. Inside, the fuel pin consists of two concentric Eurofer cylinders (outer: ⌀= 60 mm, t = 4 mm; inner: ⌀= 16 mm, t = 6 mm) joined by a bell-shaped funnel behind the First Wall.

Coolant flow scheme

Helium enters each blanket segment from the back support structure (BSS) at 300 °C and 8 MPa. It first cools the FW, exiting at 370 °C before entering the pin input channels, flowing towards the FW, and then returning via the annular outlet channels. The coolant is collected at the BSS outlet manifold at 520 °C. The tritium bred within the pins is extracted by a separate helium purge loop, as indicated in Fig. 7.

3.3.2. Tritium breeding ratio calculation

The antenna reduces the blanket volume in its vicinity and consequently the tritium breeding. A key requirement for DEMO is maintaining tritium self-sufficiency, quantified by the tritium breeding ratio (TBR) — the ratio of tritium produced in the blanket to incident neutrons. Although the ideal TBR is 1.0, the EU DEMO target is 1.15 to account for neutron losses [11]. To evaluate the impact of the antenna, we built a neutronic model using the Monte Carlo N-Particle Transport code (MCNP5) [18]. Two configurations were studied: a blanket segment with antenna and one without. Geometry: KIT provided a DEMO sector CAD model with all tokamak components, and we integrated the antenna's CAD model in this using CATIA [19], before simplifying the geometry using ANSYS SpaceClaim [20] to facilitate proper conversion of the CAD model into the MCNP format. The simplified regions of the blanket segment are shown in Fig. 8a in an exploded format, while Fig. 8b,c show them assembled. This includes eliminating all geometry features that could cause issues when converting CAD files to MCNP format, such as spline surfaces. The simplified CAD models were later converted to the MCNP format using the McCAD [21] conversion tool. Fig. 9 shows the conversion steps from CAD to MCNP. The converted model covered a single DEMO sector (three outboard and two inboard blanket segments), including the vacuum vessel, thermal shield, divertor, magnets, and upper port coolant pipes.

Materials: Because of the structural complexity of the breeding blanket and the time constraints of the project, a simplified homogenized-material approach was adopted. That is, we treated the breeding blanket as a hollow volume, then filled it with a homogeneous material mixture reflecting the ceramic breeders, neutron multipliers and Eurofer steel. This approximation is justified because our study focuses on the relative difference in TBR (ΔTBR) between the two models (with and without antenna), not the actual absolute TBR values. All other reactor components (magnets, divertor, thermal shield, etc.) were represented with their respective materials. Table 2 indicates the mixture of materials used for the study.

Neutron source: We defined a 14 MeV neutron source within the MCNP input file, with cross-sectional nuclear reaction data taken

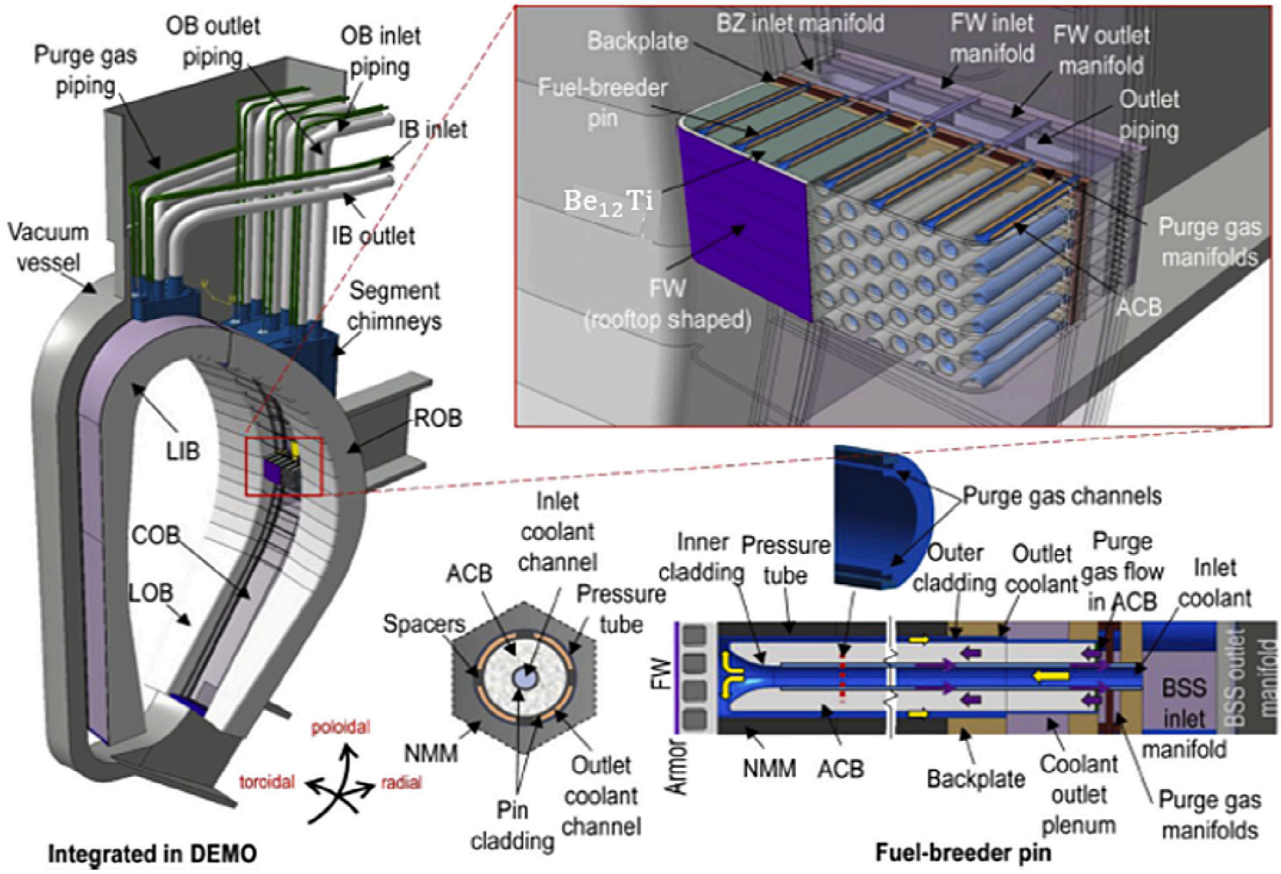

Fig. 7. Layout of the HCPB BB. Modified from [12, Fig. 1]. OB is short for Outboard, IB for Inboard. The L, C, and R before both acronyms indicate directions: L for left, C for central, and R for right, looking from the plasma end.

Table 2
Material mixtures used for the TBR study.

Component	Material	Volume fraction (%)
Tungsten layer	Tungsten	100
First Wall	Eurofer	59.4
	Helium	40.6
Breeder zone	Eurofer	8
	Helium	37.6
	Li_4SiO_4	11.7
	$Be_{12}Ti$	42.7
Back plate	Eurofer	50.7
	$Be_{12}Ti$	11.7
Back supporting structure	Eurofer	69
	Helium	31

Table 3
Reduction in TBR due to antenna integration.

Configuration	TBR value	% change in TBR
No antenna	1.20	–
Antenna	1.175	↓2%

from the FENDL reaction library [22]. The resulting neutron flux in the antenna vicinity is shown in Fig. 10. We then defined the proper neutron tallies inside the MCNP input file and performed an initial test run to diagnose whether the geometry conversion was performed properly. This was assessed by counting the number of lost neutrons in the simulation. Ideally, there should be zero neutrons lost if the conversion is done properly, which the test run indeed confirmed.

The reduction in TBR, or Δ TBR between the two models – with and without antenna – was calculated, and the results are summarized in Table 3. For a complete 360° antenna, the Δ TBR penalty is 2%. For a 180° array (i.e., an array toroidally covering half of the blanket segments), the reduction becomes ≈1%. The 2% represents the maximum Δ TBR penalty for the integration of the antenna (straps and transmission lines) within the blanket (including the reduction in blanket volume due to the recess). In absolute terms, the TBR drops from 1.20 (without antenna) to 1.175 (with antenna), still satisfying the requirement of a TBR ≥ 1.15.

The absolute TBR values in Table 3 should be interpreted with caution, as the present MCNP model uses a homogenized representation of the HCPB blanket. The main purpose of the calculation is therefore to estimate the relative TWA-induced TBR penalty, rather than to provide a final absolute TBR qualification. For comparison, recent EU-DEMO HCPB neutronic studies report an achievable TBR of approximately 1.20 at the end of the pre-conceptual design phase [23, page 13], which is above the DEMO TBR requirement of approximately 1.15 [11, page 5]. Studies of DEMO in-vessel component integration have also shown that auxiliary-system blanket cut-outs can reduce the HCPB TBR by approximately 11% [24, table 2]. In this context, the approximately 2% TWA-induced reduction obtained in the present work is modest, although not negligible.

As a simple sensitivity check, applying an 11% auxiliary-system penalty and an additional 2% TWA penalty to a baseline HCPB TBR of 1.20 gives a remaining TBR of approximately 1.04–1.05. If the TWA penalty is conservatively increased from 2% to 3% to account for the uncertainty associated with the present homogenized model, the corresponding TBR becomes approximately 1.03–1.04. These estimates indicate that while the TWA-induced penalty is relatively small compared with the penalty associated with the full set of auxiliary-system cut-outs, it also indicates that the available TBR margin can

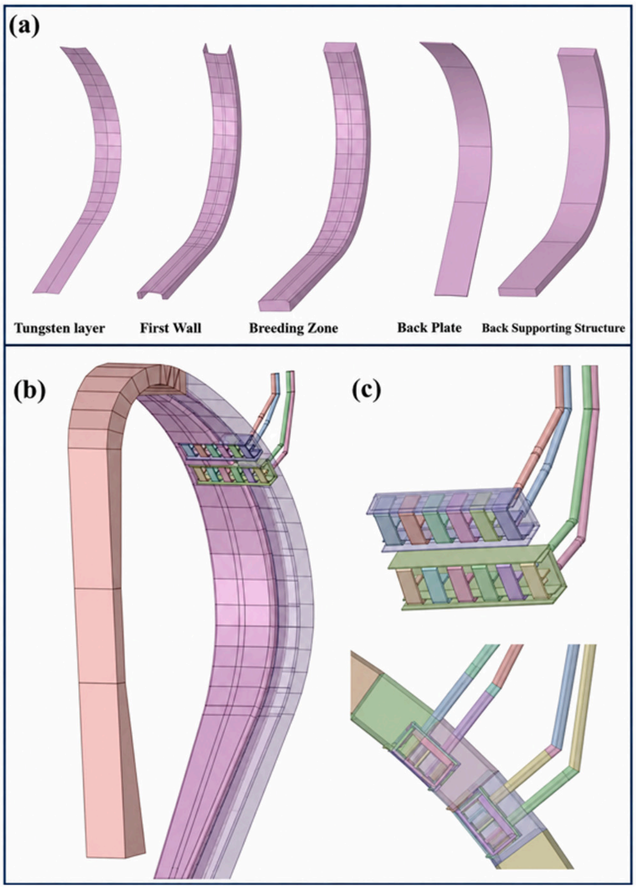

Fig. 8. (a) simplified CAD models of the five zones comprising the blanket segment, (b) simplified blanket sector geometry with the integrated antenna, and (c) simplified antenna-transmission-lines model.

become tight in conservative integration scenarios. Final confirmation of TBR compliance therefore requires a detailed heterogeneous neutronic model including the TWA geometry together with the relevant DEMO auxiliary-system cut-outs. It should also be noted that the 2% penalty corresponds to a full-ring TWA configuration. For reduced toroidal coverage, such as a half-ring configuration, the TBR penalty is expected to decrease approximately in proportion to the antenna coverage. Intermediate array configurations are also possible, in principle, and could be considered if the final TBR margin becomes restrictive.

Open points: the neutron streaming through antenna and transmission lines should be evaluated, particularly the potential impact on the superconducting magnetic field coils. If the impact is deemed unacceptable, mitigation steps should be implemented, including, e.g., installing transmission lines behind the antenna in a dog-leg configuration to prevent direct streaming, or adding extra shielding at impacted areas to limit the exposure.

4. Integration in the blanket: Antenna

Following remote handling and tritium breeding assessments, we now focus on the integration of straps within the blanket, while transmission-line (TL) integration is addressed separately in Section 5. In this section, we performed thermo–hydraulic (TH) analysis of the straps and the breeding blanket, which has been modified as a result of the antenna integration. For the TH model, a reference slice 125 mm-thick was extracted from the breeding blanket model and selected for integration studies (as indicated in Fig. 11), as this is the minimum thickness that captures all the blanket components relevant to the analysis. We then modified this slice to accommodate the antenna straps, resulting in a reduction of the depth of the slice (radial direction) by 50% and a recessed First Wall (FW) that is now behind the straps.

4.1. Antenna cooling — straps

4.1.1. Modification of pins' radial build to permit strap cooling

Building on the previously described cooling configuration of blanket pins (Section 3.3.1), the antenna straps are cooled by helium from the blanket, with local modifications to the pin cross-section. As shown in Fig. 12, each modified pin now contains two concentric helium inlet channels. The innermost channel cools the strap ("strap coolant inlet"), while the surrounding annular channel supplies helium to the pin ("pin coolant inlet"). After the strap is cooled, the helium flows out of the adjacent pin and returns to the blanket outlet manifolds. The two concentric coolant channels are thermally decoupled by a thin stagnant helium gap (0.5 mm) within the Eurofer jacket that separates both channels (depicted in Fig. 12 as "strap inlet pressure tube"), a technique also used for manifold isolation in the blanket.

4.1.2. Integrated view of modified pins with the reference blanket slice

Fig. 13 illustrates the modifications implemented in the blanket to facilitate the cooling of the strap. The reference slice (panel a) includes a front region with the First Wall (FW), neutron multiplier material (NMM), and breeder pins, and a rear region containing the coolant inlet/outlet manifolds, collectively termed the back support structure (BSS). Panels b–c show the integrated strap configuration with the modified breeder pins visible. Compared with the original blanket slice, the modified pins now feature a thinner breeding zone to accommodate an additional cooling channel (see also Fig. 12). The main characteristics of the modified slice are as follows:

- a shortened breeding zone (illustrated by panels (a) and (b) in Fig. 13, the breeding zone being brown)
- recessed FW behind the straps and
- two concentric coolant channels in 16 pins per blanket segment (out of $\approx$ 1875 total pins per blanket segment, as Fig. 12b illustrates)

The BSS manifolds are divided into two systems: (i) FW coolant inlet/outlet and (ii) breeder-zone coolant inlet/outlet. As shown in Fig. 13c, the modified pins, located behind the straps, connect to these manifolds through extended "tongues" to the FW inlet manifold chamber (FIMC) and shortened tongues connected to the breeding outlet manifold chamber (BOMC). This architecture is further detailed in Figs. 13–14. The modifications also reduce the volume of the purge gas manifold chambers surrounding the affected pins. Accordingly, the impact on purge gas performance is expected to be small, although this should be confirmed in future dedicated analysis.

4.1.3. Coolant flow paths and parameters inside pins and straps

Fig. 14 illustrates the coolant flow path for a strap. For the thermo–hydraulic assessment, a sub-model was cut-out from the modified blanket slice, which retains all the essential components. These sub-models are shown in Fig. 14c,d. For TH analysis, the following boundary conditions apply:

Pins: helium enters at 370 °C and 8 MPa. The only modification is in the geometry of coolant channels, with two concentric inlet channels (an innermost circular channel surrounded by an annular one) instead of a single inlet channel. The channel dimensions were configured to maintain flow velocities and pressure drops comparable to those of the original pin design.

Straps: coolant enters through a dedicated pipe (Fig. 14(d) from the First Wall inlet manifold chamber (FIMC) at 300 °C and 8 MPa and is distributed inside the strap through the 'cold' chamber of a

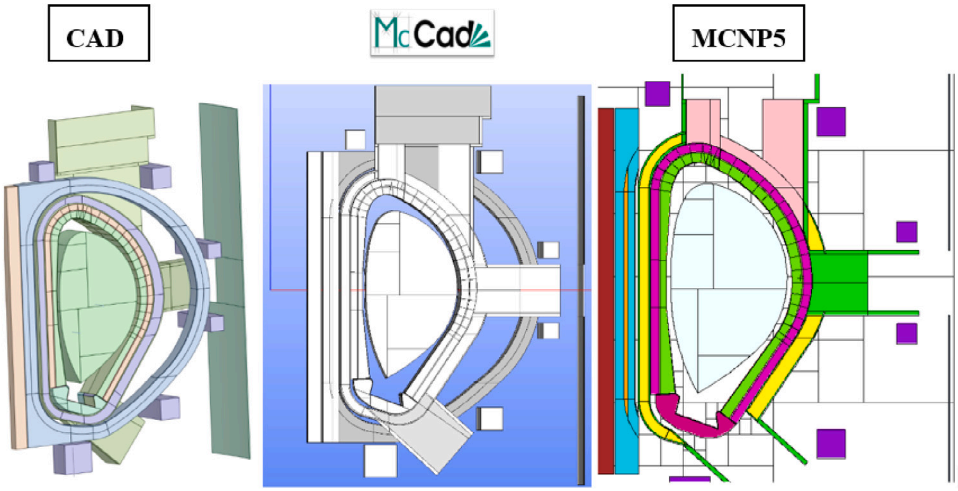

Fig. 9. Geometry conversion steps – for the case without antenna – from CAD format to MCNP format using McCAD tool.

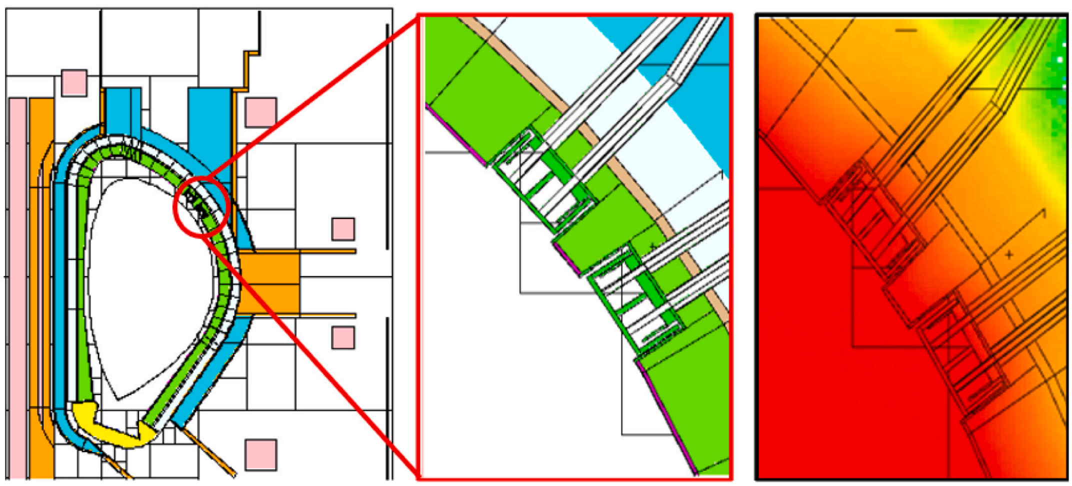

Fig. 10. Left: MCNP plot of the converted geometry with antenna. Middle: zoomed view of the converted antenna geometry, with the straps and transmission lines visible. Right: corresponding neutron-flux map in the antenna vicinity, shown on an arbitrary scale.

distributor manifold that replicates the geometry of the First Wall (see Fig. 14(f). Upon exiting the strap, an adjacent 'hot' chamber in the distributor manifold redistributes the heated coolant back into the blanket outlet manifolds. This general configuration was optimized to maintain a maximum temperature and a drop in coolant pressure in each strap at $T_{max} < 550$ °C and $\Delta p \leqslant 5$–10 kPa, respectively. A detailed thermo–hydraulic analysis of this configuration is presented below.

4.1.4. Thermal–hydraulic loads, boundary conditions, and results

The thermo–hydraulic (TH) model proposed in Fig. 14 was analyzed using ANSYS CFX V19.2 to calculate the temperature fields, the coolant flow and the pressure drop. Two types of thermal loads were considered. Under normal operation, surface loads arise from plasma radiation and charged particle flux. In EU DEMO, the latter is largely mitigated by limiters [25], leaving plasma radiation as the dominant contribution. A combined surface heat flux of 0.25 MW m^{-2} was applied to the front face of the strap, consistent with [26, Fig. 5]. The horizontal strap section is shadowed by overlying blanket boxes and therefore is assumed to be load-free, according to [26]. In addition, volumetric heating due to neutron interactions within the strap was applied using a quasi-exponential profile as in Fig. 15, bottom panel, based on the profiles in [15, Fig.5]. For the breeding zone, thermal loads were limited to neutron-induced volumetric heating, as plasma radiation is fully shielded by the First Wall.

Table 4
Boundary conditions for strap thermal–hydraulic analysis.

Parameter	Value	Unit
Inlet pressure	8	MPa
Inlet temperature	300	°C
Mass flow rate	62	g/s
Channel roughness	6.8	μm

For the thermal–hydraulic analysis of the strap, helium inlet conditions of 8 MPa and 300 °C were imposed, consistent with the First Wall coolant manifold. The flow rate of the strap coolant mass was fixed at 62 g s^{-1}, determined by successive simulation iterations to balance temperature and pressure drop. The wall roughness of the strap's coolant channels was set at 6.8 μm, identical to the FW channels. A summary of the boundary conditions is given in Table 4.

For breeding pins, the coolant entry conditions were roughly 8 MPa and 370 °C, reflecting a drop in the coolant pressure of 390 Pa and a heating from 300 to 370 °C through the FW, while the flow rate at the outlet was set at 15.6 g s^{-1} [15]. A wall roughness of 44 μm and 6.8 μm were applied to the outer and inner coolant channels, respectively [14, 15]. Using poloidal symmetry, only half of the geometry was modeled to reduce computational cost. Table 5 summarizes those parameters.

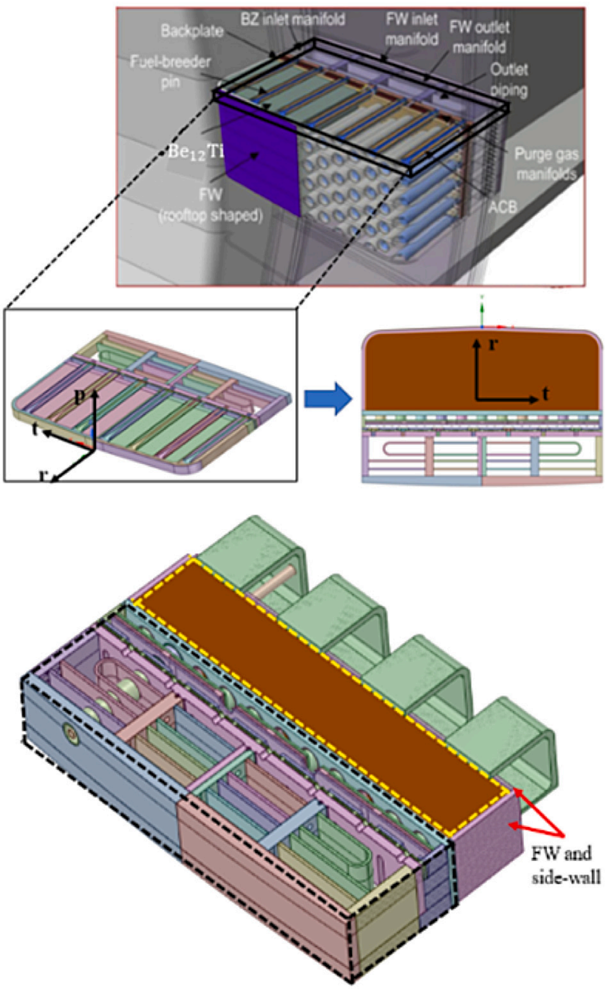

Fig. 11. Reference blanket slice extracted from the outboard blanket (top) and used as the basis for the thermo–hydraulic analysis. The slice is subsequently modified to accommodate the straps (bottom). The letters t, r, and p denote the toroidal, radial, and poloidal directions, respectively.

Table 5
Boundary conditions for pins thermal–hydraulic analysis.

Parameter	Value	Unit	Notes
Inlet pressure	8	MPa	
Inlet temperature	370	°C	
Mass flow rate	15.6	g/s	obtained from [15]
Channel roughness	6.8	μm	inner channel walls
Channel roughness	44	μm	outer channel walls

Table 6
Thermal–hydraulic analysis results.

Parameter	Value	Unit	Margin (%)	Component
Max temperature	495	°C	+10	strap
	633	°C	+31	breeding zone
	926	°C	+2.5	neutron multiplier
	375	°C	/	outlet helium
Pressure drop	5.6	kPa	/	strap coolant
	2.5	kPa	/	modified pins coolant

With these boundary conditions, the maximum strap temperature was ~495 °C (Fig. 16), corresponding to ~90% of the Eurofer design limit (550 °C), i.e. with a remaining (positive) margin of ~55 °C (10%). A non-symmetric temperature profile is observed on the strap front face, due to uneven coolant distribution among channels. This could be improved by modifying the geometry of the FW-like distributor, e.g., gradually varying the interfacing geometry instead of the abrupt cylindrical to rectangular transition. The average helium temperature of the strap outlet – which, when exiting, is reinjected to cool the pins of the breeding zone – was 375 °C, very close to the 370 °C cooling injection temperature of the breeding zone. The pressure drop across the strap circuit was $\Delta p \approx 5.6$ kPa, on par with the original blanket pins ($\Delta p \approx 5$ kPa), showing satisfactory hydraulic behavior.

Table 7
Structural design criteria used for structural analysis.

Stress component	Stress-limit expression	Failure mode
Primary membrane	$Max\overline{(P_m)} \leq \overline{(S_m)}$	IPC
Membrane+bending	$Max\overline{(P_m + P_b)} \leq 1.5\overline{(S_m)}$	IPI
Membrane+secondary	$Max\overline{(P_m + Q_m)} \leq 1.5\overline{(S_m)}$	IPFL

Fig. 17 shows the temperature distribution in the components of the breeding zone, the Li_4SiO_4 breeder, and the $Be_{12}Ti$ neutron multiplier, respectively. The maximum Li_4SiO_4 temperature is 633 °C, which corresponds to roughly 69% of the design limit (920 °C), i.e. a remaining margin of 287 °C (~31%), while the maximum temperature of $Be_{12}Ti$ is 926 °C, corresponding to 98% of the design limit (950 °C), leaving a margin of 24 °C (~2.5%). The pressure drop across the modified pin was 2.54 kPa, approximately half that of the original design, due to its reduced effective length. The results of the thermal–hydraulic analysis are summarized in Table 6.

4.1.5. Structural loads, boundary conditions, and results

The breeding pins remain structurally unchanged in our integration scenario, apart from being now shortened behind straps. As they are cantilevered components from the back of the blanket segment (see Fig. 7, bottom-right), shorter pins are expected to be even stiffer than the original longer pins. Structural assessment therefore focused on straps under normal operating conditions; off-normal events such as seismic loading or plasma disruptions were not included at this stage. However, plasma disruptions are not expected to affect straps, since eddy current loops require at least two contact points with the blanket [27], whereas straps are connected at only one.

Loads and methodology: primary loads included an 8 MPa coolant pressure applied to the internal cooling channels and the self-weight of the strap. Secondary loads were given by the thermal profiles in Fig. 15. The analysis was performed with ANSYS Workbench Mechanical v19.2 [28], following the RCC-MRx rules [29].

Boundary conditions: the strap surface in contact with the blanket had all nodes radially constrained, with toroidal and poloidal displacements allowed in all other nodes. To prevent rigid-body motion and strap rotation, two corner nodes on the same face were additionally constrained in the toroidal and poloidal directions.

Failure modes: Immediate monotonic damage modes were considered: Immediate Plastic collapse (IPC), Immediate Plastic Instability (IPI) and Immediate Plastic Flow Localization (IPFL). Table 7 summarizes the structural design criteria considered under RCC-MRx for monotonic damage modes, with $\overline{(P_m)}$ being the average primary membrane stress intensity, $\overline{(P_m + P_b)}$ the average primary membrane and bending stress intensities, and $\overline{(P_m + Q_m)}$ the average primary and secondary membrane stress intensities, while $\overline{S_m}$ is the average allowable design stress intensity, typically set at two thirds of the yield stress for ductile materials. Fig. 18 shows the resulting stress distribution. The maximum primary von Mises stress intensity was 90 MPa, found at one of the two constrained corner nodes (Fig. 18, top). The temperature at that point is 345 °C, where the stress intensity allowed is $\overline{S_m} \approx$ 135 MPa. This stress field already encompasses both the membrane and

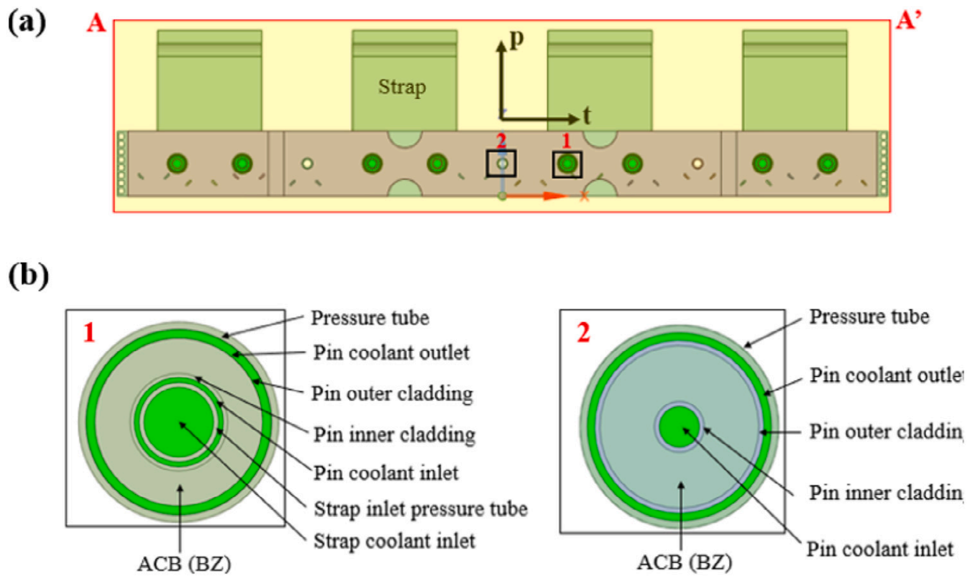

Fig. 12. (a) modified blanket slice viewed from the back of the blanket segment (cutting plane A–A' is indicated in Fig. 13(b), (b) insets 1 and 2 compare the modified and original pin cross-sections, respectively. The overall pin's size and diameter remain unchanged, but the coolant inlet is reconfigured into two concentric channels: the innermost is dedicated to strap cooling, while the other is dedicated to the pin. Acronyms: ACB — Advanced Ceramic Breeder; BZ — Breeding Zone.

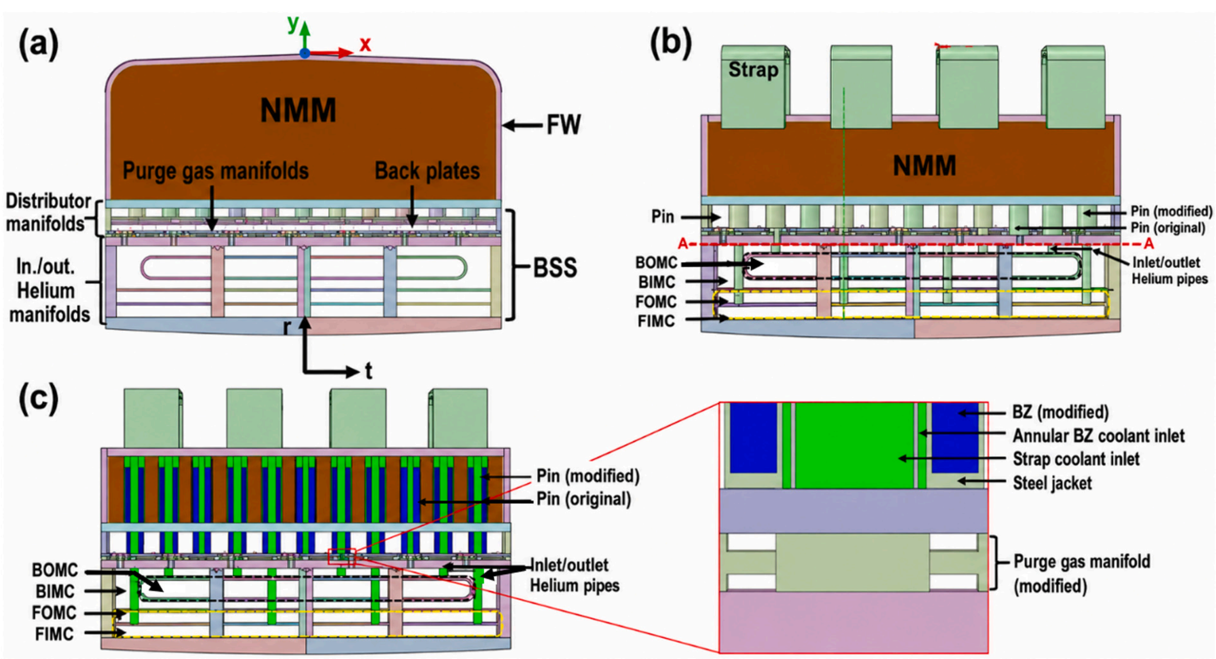

Fig. 13. Blanket-slice configurations: (a) top view of the original slice, (b) top view of the modified slice with straps, (c) bottom view of the modified slice, including a detail of the pin–purge-gas interface region. Acronyms: BOMC — Breeding zone Outlet Manifold Chamber, BIMC — Breeding zone Inlet Manifold Chamber, FOMC — First Wall Outlet Manifold Chamber, FIMC — First Wall Inlet Manifold Chamber, and BZ — Breeding Zone.

the bending stress components, which means that both the IPC and IPI criteria are satisfied. For IPFL assessment, both primary and secondary stresses were extracted along a path that crossed the critical section, i.e., that part of the strap that contains the most stressed point (Fig. 18, middle). At that point, the temperature was found to be 400 °C from the previous thermal analysis, which corresponds to $\overline{S_m} \approx 127$ MPa, giving $1.5\overline{S_m} \approx 190$ MPa. The results in Table 8 confirm that the IPFL criteria are met. The combined loading produced a maximum deformation below 1 mm (Fig. 18, bottom).

Table 8
Structural analysis results for the IPFL damage mode.

$Max\overline{(P_m + Q_m)}$	T at stress max. [°C]	$1.5\overline{S_m}$ at 400 °C [MPa]
104	400	190

4.2. Straps integration: Open points and a future outlook

Thermal–hydraulic analysis did not include transient thermal loads, in which heat fluxes of up to 1 MW m^{-2} [15] could appear on the

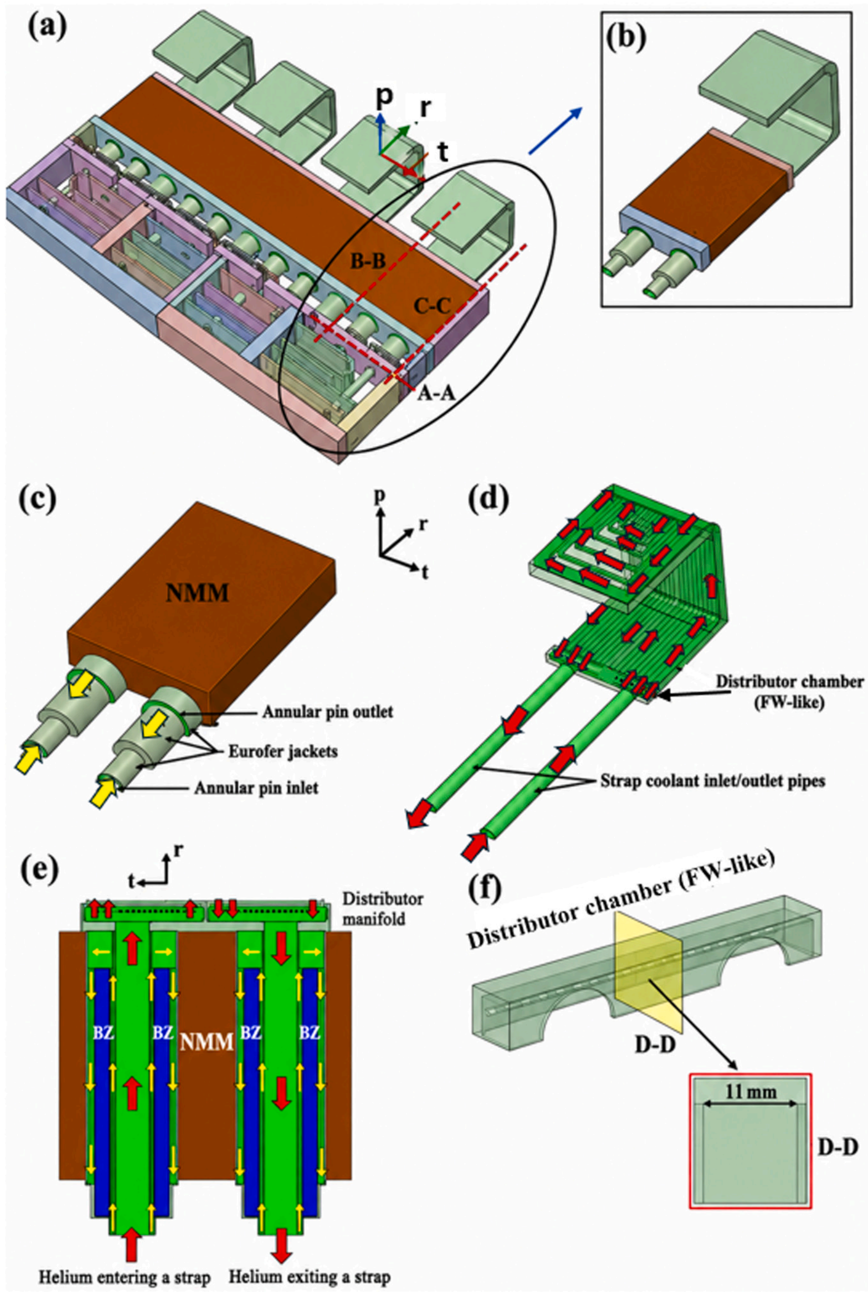

Fig. 14. (a,b) Modified blanket slice and derived sub-model used for the thermo–hydraulic analysis. (c,d) Decoupled views of the same sub-model, showing the pin and strap thermo–hydraulic domains separately. (e) Bottom view of the sub-model, with the strap hidden, illustrating coolant flow paths in the pins (yellow arrows) and straps (red arrows). (f) FW-like distributor manifold behind the strap.

First Wall, dominated by charged particle flux. An extended TH analysis should explore the cooling of straps at such heat fluxes. Previous studies indicated that a helium cooled surface could handle up to 3 MW m^{-2} if the cooling channels were configured with ribs [30], and a similar approach could be applied for straps if needed. The installation of a Faraday Shield (FS) could be another option for antenna shielding [31]. Fig. 19 illustrates a possible FS configuration. Future work should investigate the transient thermo–hydraulic performance of straps incorporating either artificial ribs or a protective Faraday shield. The structural analysis could be extended to more general loading cases, such as seismic events, which were not covered in the present analysis. In addition, a future high-heat-flux case study is required to ensure strap integrity during peak plasma operations.

5. Integration in the blanket: Transmission lines

5.1. Integration strategy in blanket

Transmission Lines (TLs) supply power to the antenna, which then radiates it into the plasma. For the DEMO layout in Fig. 2, calculations indicate that eight TLs (outer diameter 76 mm) per vertical port are required [13]. This dimension is comparable to the outer diameter of the pressure tubes of the blanket (82 mm), allowing a one-to-one substitution: eight pins are replaced by eight TLs per blanket sector. Given 90,000 pins in DEMO (5625 per blanket sector) [15], replacing only 8 pins per sector explains the limited impact on TBR reported earlier in Section 3.3 even when TLs are considered. Fig. 20 illustrates this substitution scenario. A blanket segment can be

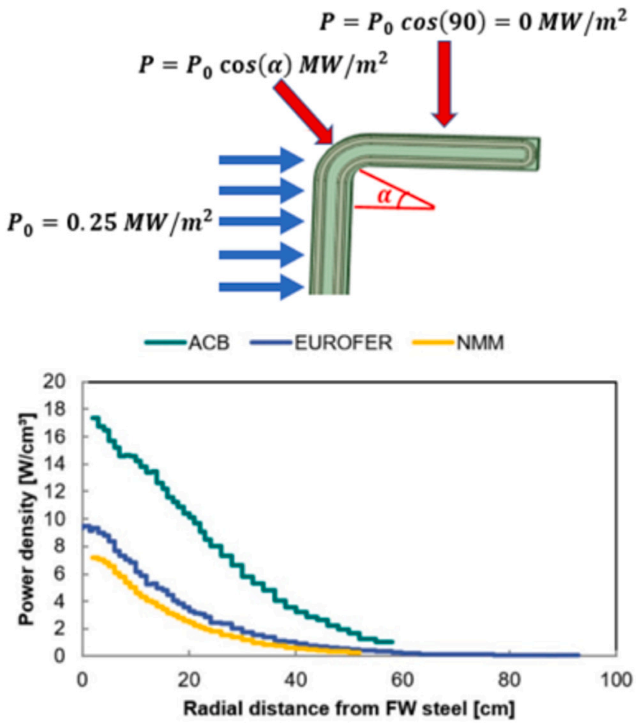

Fig. 15. Heat flux profile on a strap (left) and volumetric radial heat profiles in breeding pins. Quoted from figure 5 in [15].

divided into two regions: (i) the front region, including the FW and breeding zone (containing pins and neutron multiplier), where the TL simply replaces a pin due to its comparable diameter; and (ii) the back region, consisting of coolant manifolds. In the back region, the TL crosses four Manifold Chambers: the First Wall Input Manifold Chamber (FIMC), the First Wall Outlet Manifold Chamber (FOMC), the Breeding-Zone Input Manifold Chamber (BIMC) and the Breeding-Zone Outlet Chamber (BOMC) (see Fig. 20(b)). Consequently, the TL is immersed in helium at markedly different temperatures (300 °C, 370 °C and 520 °C). Although this provides effective cooling, it may also introduce thermal stresses. To mitigate these stresses, thermal isolation is proposed between TL and FIMC (300 °C) and BOMC (520 °C). This can be achieved by inserting a thin (2 mm) Eurofer sleeve around the TL in these regions, which contain stagnant helium at 370 °C. Therefore, in the back manifold region, direct thermal contact between the TL and the coolant is maintained only in the FOMC and BIMC (both at 370 °C), thus homogenizing the thermal profile of the TL and minimizing Δ Tmax across the TL in that region. This thermal decoupling strategy has already been applied elsewhere in the blanket [32].

Integration of the front region and cooling of the inner conductor: In the front region, each TL occupies the volume of a single pin (Fig. 20d and Fig. 21). Helium, entering from the BIMC at 370 °C (yellow arrows at the entrance of the annular cooling outlet, indicated in Fig. 20(d), flows through the TL through an annular channel formed between the outer conductor of the TL and a cylindrical shell that separates the flow (indicated more clearly in Fig. 22(c). Then it turns 180° near the FW, returning through a second annular region between the shell and the pressure tube's wall, before exiting the BOMC and mixing with the outlet flow of the blanket (Fig. 20(d).

Within the blanket, the TL consists of an outer conductor extending from the BSS to the FW, and an inner conductor that penetrates the FW to connect mechanically and electrically to the strap. Active cooling of the inner conductor is expected to be more demanding, as it is fully enclosed by the outer conductor, thus limiting direct helium access.

Table 9
Boundary conditions for TL's outer conductor TH analysis.

Parameter	Value	Unit	Notes
Inlet pressure	8	MPa	/
Inlet temperature	370	°C	/
Mass flow rate	10	g/s	obtained iteratively
Inner channel roughness	6.8	µm	see Fig. 22c
Outer channel roughness	44	µm	see Fig. 22c

Alternatively, passive cooling of the inner conductor by radiation alone is investigated in Section 5.3.

Fig. 21 illustrates an isometric view of the front of an integrated TL (orange). The TL–strap connection is expected to have a conical "tap" shape, although the exact geometry remains undefined. Finalizing this interface is critical not only to assess the viability of using strap coolant as an inner conductor cooling option but also to assess the structural integrity of the inner conductor–strap joint. Therefore, future studies are required to optimize the thermal–hydraulic and mechanical design of this region once the geometry is clarified.

5.2. Outer conductor cooling

5.2.1. Thermal–hydraulics: Geometry, loads, and boundary conditions

Fig. 22 shows the CAD geometry for the thermal–hydraulic analysis. Using geometric symmetry, the basic cooling model was extracted (Fig. 22b, c). The radial structure (Fig. 22(c) comprises: the outer TL conductor at the core, an annular helium input channel (green), a steel jacket or cylindrical shell separating the inlet and outlet channels, and an annular helium outlet channel (green) bounded by the pressure tube wall. The latter prevents direct contact between the coolant and the surrounding neutron multiplier (brown). Volumetric heating was applied to the Eurofer body of the TL using the "Steel" neutron heating profile of Fig. 15. The power dissipation from RF operation was not included in this calculation, as it is not expected to be the driving force of the design at this stage [13]. The boundary conditions consisted of helium entering the inlet channel at 370 °C and 8 MPa, with a mass flow of 10 g/s. This flow rate was determined iteratively to ensure that all components remain below allowable temperature limits while minimizing pressure losses. The applied boundary conditions are summarized in Table 9.

5.2.2. Thermal–hydraulic results

Thermal–hydraulic (TH) results are presented in Fig. 23. The maximum temperature of the outer conductor is 446 °C (left panel), while the neutron multiplier reaches 868 °C (right panel). Both values remain within the respective design limits (550 °C for the Eurofer and 920 °C for the neutron multiplier). The helium outlet temperature is 437 °C, with a pressure drop of 4.7 kPa, comparable to that of a breeding pin (5 kPa). However, the temperature of the outlet helium coolant differs significantly: approximately 440 °C for a TL versus 550 °C for a pin. This reduction is due to much lower volumetric heat generation in the Eurofer steel body of TL compared to the ceramic breeder, which is consistent with the profiles in Fig. 15. From the perspective of the blanket-segment, the localized reduction in the outlet temperature is acceptable [33]. The total helium mass flow rate per outboard blanket segment is approximately 30,000 g/s while only 80 g/s is required for 8 TLs, which represents less than 0.3% of the total segment flow. Consequently, any local thermal perturbations in the outlet helium temperature are expected to be rapidly smoothed out upon mixing with the coolant in the full blanket segment. The thermal–hydraulic performance of the integrated TL outer conductor can therefore be regarded as favorable. Table 10 summarizes the results.

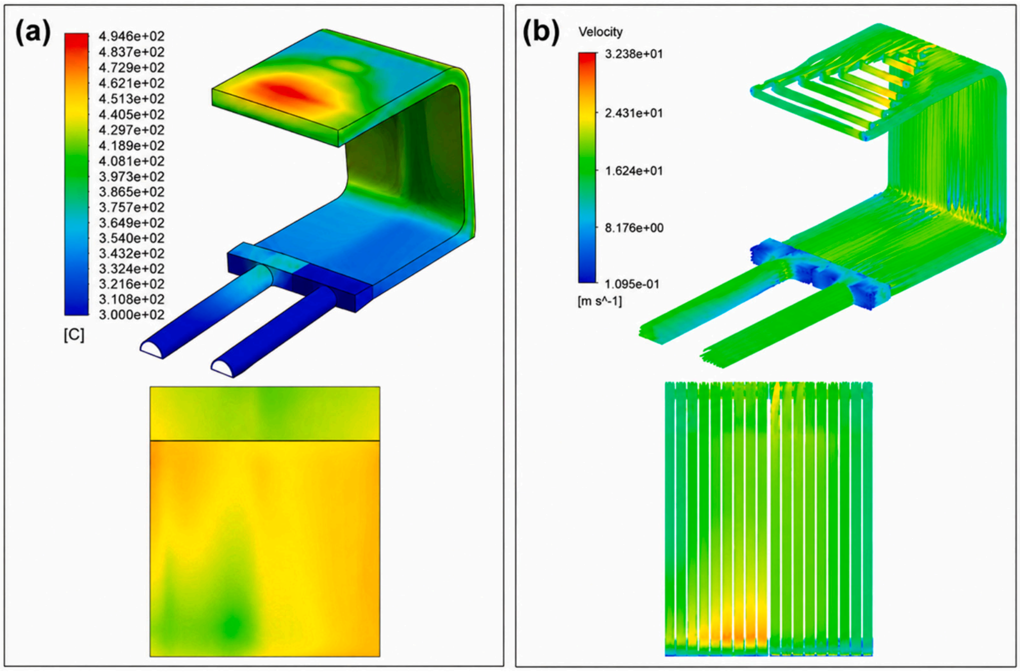

Fig. 16. (a) Temperature distribution in the strap, distributor manifold, and inlet/outlet pipes (top), and the strap front face (bottom), (b) coolant streamlines and flow velocities. Only half of the geometry is shown owing to symmetry.

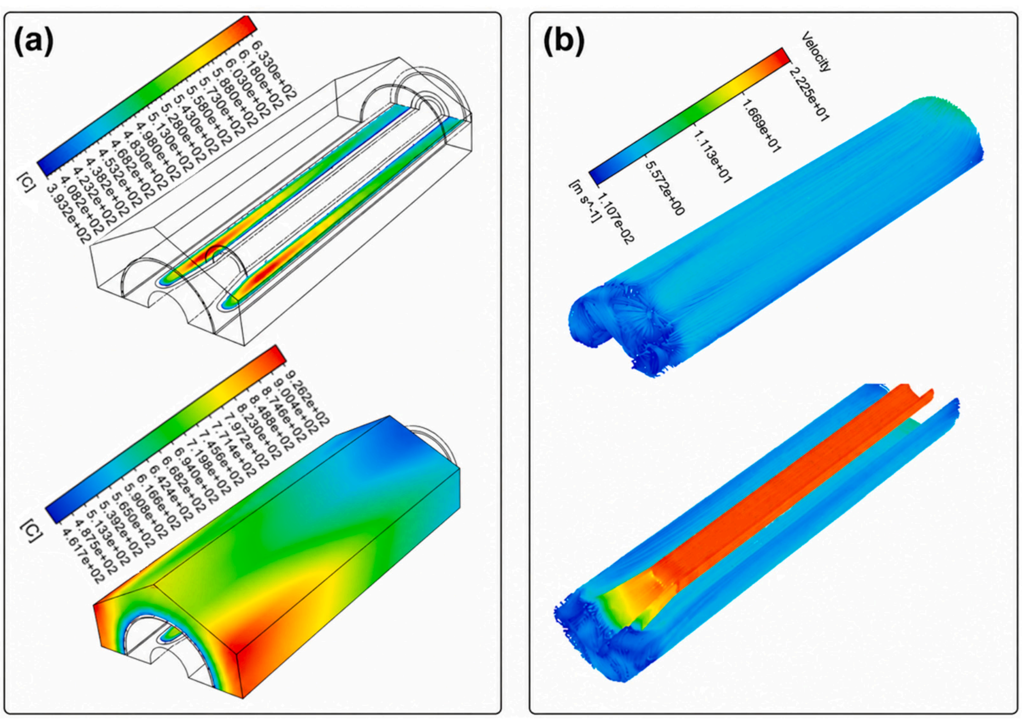

Fig. 17. (a) Temperature distributions in the breeding zone (top) and neutron multiplier (bottom). The highest temperatures occur on the front side, i.e. the side closest to the plasma, (b) exploded view of the pin showing the upper and bottom halves with the coolant streamlines and flow velocities.

5.3. Inner conductor cooling

Active cooling of the inner conductor is more challenging because it is enclosed within the outer conductor. Three potential active-cooling options were considered: (i) sharing strap coolant with the inner conductor, (ii) sharing First Wall coolant with the inner conductor, and (iii) introducing coolant channels within the inner conductor body, with coolant supplied through the insulator rods between the inner and outer conductors. Option (i) appears to be the most attractive, but it depends critically on the geometry of the TL–strap interface, which has not yet been defined. Option (ii) takes advantage of the inner conductor passing through the FW but could disrupt the continuity of the FW cooling scheme. Option (iii) is constrained by the currently undefined design of the dielectric insulators and their compatibility with active cooling. Given these uncertainties, only a passive cooling concept is assessed in the present work. In this scheme, which extends

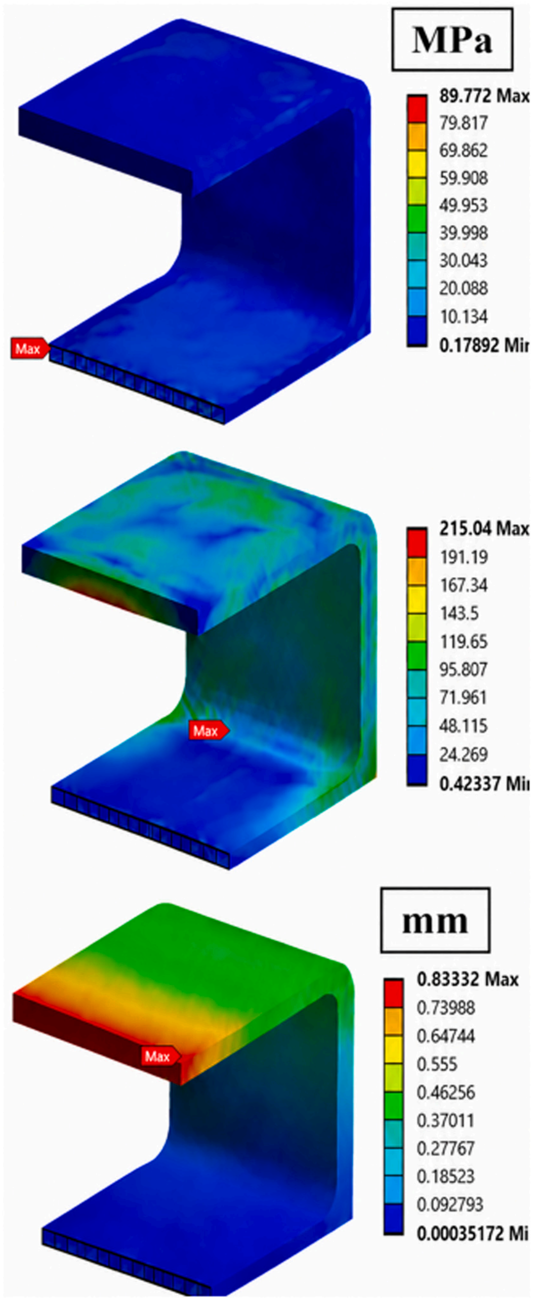

Fig. 18. Von Mises stress field due to primary loading (top) and combined primary and secondary loading (middle). Total deformation under combined loading is at the bottom.

Table 10
Thermal–hydraulic results for the TL's outer conductor.

Parameter	Value	Unit	Component
Max temperature	446	°C	Outer conductor
	868	°C	Neutron multiplier
	437	°C	Outlet helium
Pressure drop	4.7	kPa	Outer conductor coolant

the analysis of the previous section by including the inner conductor, heat is removed from the inner conductor by radiative exchange with the outer conductor (Fig. 24). An emissivity range of 0.25 to 0.8 was assumed for stainless steel, with a nominal value of 0.5 [33]. The corresponding boundary conditions are listed in Table 11. The analysis

Table 11
Boundary conditions for TL's inner conductor radiation cooling analysis.

Parameter	Value/type	Unit	Notes
Roughness	6.8	μm	conductor's surface
Emissivity	0.25,0.5,0.8	/	values from [33]
Viewing factor	surface to surface	/	between conductors
Dielectric medium	vacuum	/	/
Conductor's thickness	3	mm	skin depth

Table 12
Maximum temperature of inner conductor for different emissivity values.

Parameter	Value	Unit	Emissivity
Max temperature	652	°C	0.25
	548	°C	0.50
	494	°C	0.80

presented below is exploratory in nature and depends on assumptions regarding inner-conductor thickness and surface emissivity. Its purpose is to provide an initial estimate of the feasibility of radiation cooling until the strap–inner-conductor interface is defined well enough for a detailed helium-cooling assessment.

The temperature distribution on the inner conductor is shown in Fig. 25, for the case of 0.5 emissivity. The maximum temperature reaches ~550 °C, approximately the Eurofer design limit. However, since this limit is primarily set to prevent thermal creep in pressurized components and since the inner conductor is unpressurized (passively cooled), higher operating temperatures (up to 650 °C) could still be acceptable [33]. The analysis assumed a 3 mm-thick inner conductor based on skin depth considerations of RF currents, where the flow of RF current is constrained within a very thin surface, much thinner than the 3 mm-thick inner conductor [13]. Structural verification will be required to confirm whether this thickness is mechanically sufficient; if not, thicker conductors may necessitate reanalysis, potentially with surface treatments (coatings, roughening) or stagnant helium gaps to enhance radiative exchange. Table 12 summarizes the maximum temperatures obtained as a function of the emissivity of stainless steel. Should future studies indicate that a 3 mm thick inner conductor does not meet structural integrity requirements and that radiative cooling is insufficient for thicker conductors, the active cooling schemes outlined earlier could be revisited.

Open points: RF dissipation was not included in the detailed thermal model because a component-level RF-loss map is not yet available. However, a simple bounding estimate was added to assess the possible magnitude of this contribution, particularly for the passively cooled inner conductor.

Assuming a total RF dissipation fraction of 2% of the 50 MW TWA power gives 1 MW of distributed RF heat. For a full-ring configuration with 16 TWA sections, 320 straps, and 128 transmission lines, this heat was first divided equally between straps and transmission lines. This gives 500 kW on the straps, corresponding to approximately 1.56 kW of dissipated RF power per strap, and 500 kW on the transmission lines. For a coaxial line made of the same material for both conductors, the RF loss per unit length is approximately inversely proportional to the conductor radius. Therefore,

$$\frac{P_{inner}}{P_{outer}} \approx \frac{r_{outer}}{r_{inner}}$$

where r_{outer} denotes the effective radius at which the RF current flows on the outer conductor. For typical ICRF coaxial impedances of about 30–50 Ω, this radius ratio is of order 1.5–2.5. Taking a representative value of 2 gives approximately two thirds of the TL conductor loss on the inner conductors and one third on the outer conductors. The resulting RF heat loads are therefore approximately 2.6 kW per inner conductor and 1.3 kW per outer conductor.

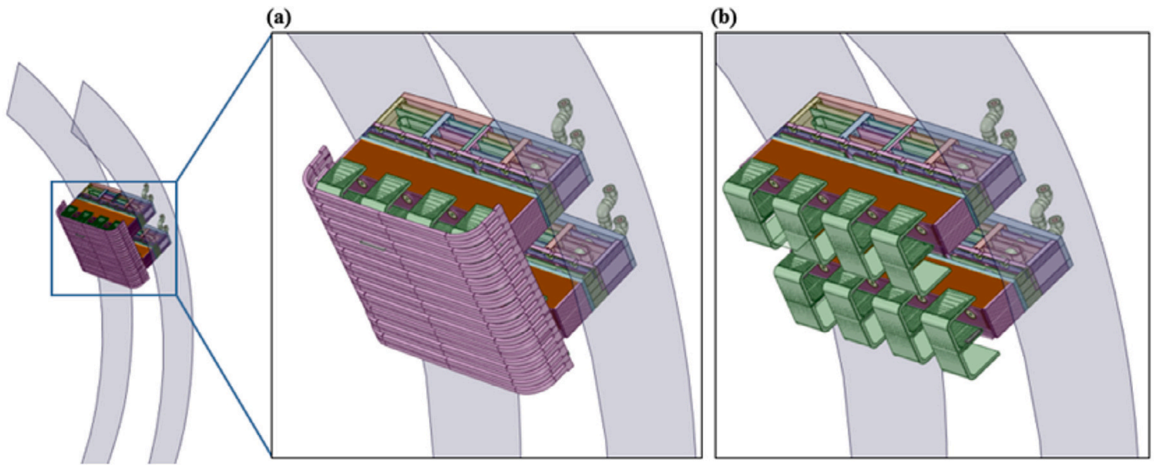

Fig. 19. One potential layout of a Faraday Shield: (a) installed, (b) not installed. Gray planes represent BB segment boundary. A Faraday shield may help screen charged-particle fluxes and optimize wave coupling to the plasma. A dog-leg transmission-line configuration is visible at the back.

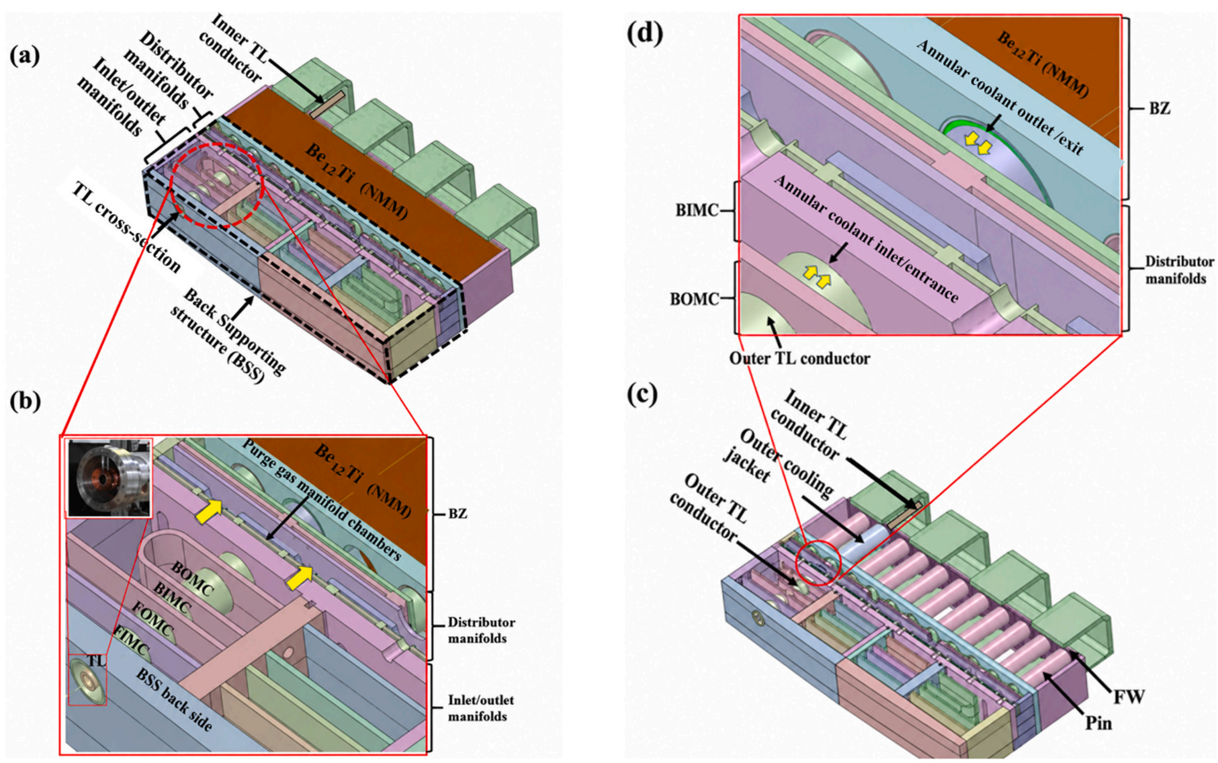

Fig. 20. (a) View of a blanket slice with an integrated transmission line. (b) Detail of the back region, where the TL passes through and is cooled by helium in the various manifolds, with yellow arrows indicating coolant flow from the back to the front regions. (c,d) Coolant-flow scheme for the TL, with yellow arrows in panel (d) indicating coolant entrance and exit locations (referred to as annular coolant inlet and annular coolant outlet, respectively) around the front part of the TL.

As an independent order-of-magnitude check, the RF loss on one inner conductor was also estimated using the standard RF surface-resistance expression

$$R_s = \sqrt{\frac{\pi f \mu}{\sigma}}$$

where f is the RF frequency, μ is the effective magnetic permeability of the conductor material at the operating frequency, and σ is the electrical conductivity. The AC resistance per unit length of the inner conductor is

$$R'_{\text{inner}} = \frac{R_s}{2\pi r_{\text{inner}}}$$

For a matched coaxial line carrying traveling power P_{line}, the RMS current is

$$I_{\text{rms}} = \sqrt{\frac{P_{\text{line}}}{Z_0}}$$

and the power dissipated on the inner conductor over length L is

$$\begin{aligned} P_{\text{loss,inner}} &= I_{\text{rms}}^2 R'_{\text{inner}} L \\ &= \frac{P_{\text{line}}}{Z_0} \frac{R_s L}{2\pi r_{\text{inner}}}. \end{aligned}$$

Using $f = 50$ MHz, $Z_0 = 50\ \Omega$, $r_{\text{inner}} \approx 15$–$16$ mm, $L \approx 0.5$ m, and $\sigma_{\text{Eurofer}} \approx 1.0$–$1.5 \times 10^6\ \text{S m}^{-1}$, gives $R_s \approx 0.011$–$0.014\ \Omega$, assuming

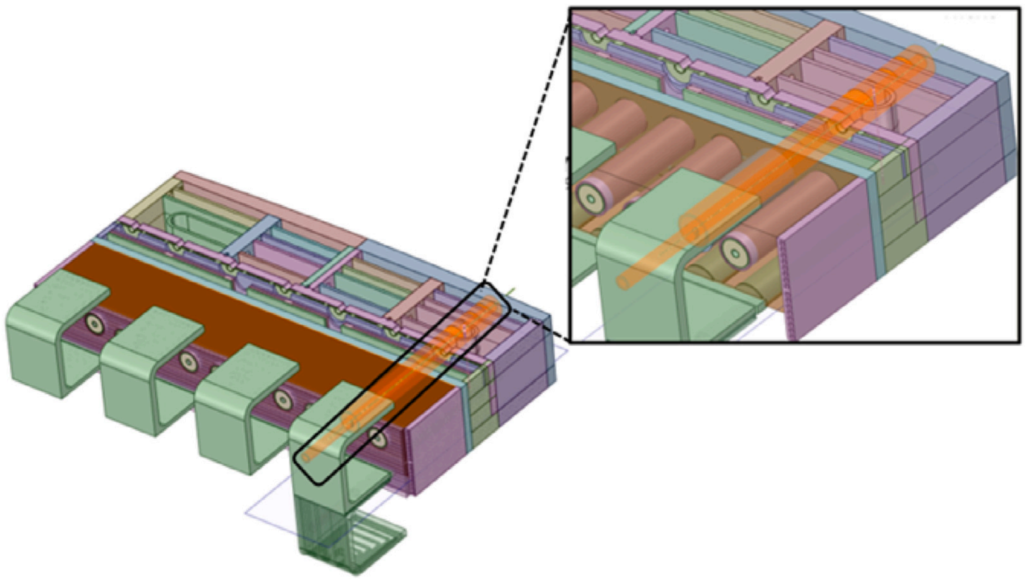

Fig. 21. Isometric, front-side view of an integrated TL (orange) in the blanket, where a single TL replaces one blanket pin. A mirrored surface has been added to the last strap on the right to show the full geometry, with the cooling channels visible in the transparent lower part.

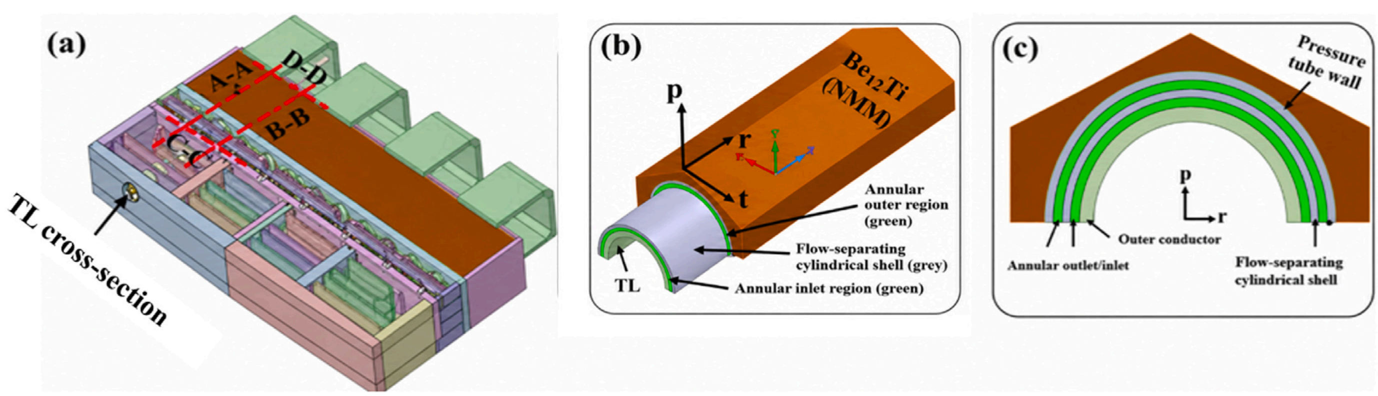

Fig. 22. (a) Thermo–hydraulic model cutting planes (A–A, B–B, C–C, D–D), (b) the resulting geometry used for thermo–hydraulic analysis (plasma side is at the top-right part of this panel), (c) front (plasma-side view) of the geometry with various components labeled.

$\mu_r = 1$ as a first-order lower-bound estimate. This corresponds to an inner-conductor resistance of approximately 0.06–0.08 Ω over the blanket-region length. For an illustrative traveling power of 1.5 MW per line, the resulting RF loss is approximately 2.4 kW on one uncoated Eurofer inner conductor. This is consistent with the 2.6 kW value obtained from the 2% system-level bounding estimate. Previous studies of TWA structures indicated total RF losses of less than 4% [34] for the entire system, a figure that was also supported experimentally [35]. While the TWA system in [35] does not exactly correspond in configuration to the TWA for DEMO, the numbers should still serve as indicators of the order of magnitude of RF losses expected in TWA systems.

These estimates indicate that RF dissipation is not expected to be dominant for the actively cooled straps or TL outer conductors, but it can affect the passively cooled inner conductor. In the present radiation-only calculation, the inner conductor reaches approximately 548 °C for $\varepsilon = 0.5$, close to the conventional 550 °C Eurofer design limit. This limit is mainly relevant for pressure-bearing Eurofer components, whereas the inner conductor is not pressure-bearing in the present integration scenario. Therefore, temperatures above 550 °C are not automatically disqualifying for this component, subject to further structural and materials verification. Nevertheless, RF dissipation could reduce the thermal margin of the passive-cooling solution. Future work should therefore include a coupled RF-loss/thermal model, and enhanced emissivity, coatings, improved radiative exchange, or active inner-conductor cooling may be required.

5.4. Integration strategy in vertical ports

Following the remote handling compatibility assessment highlighted in Section 3.2, this section outlines the routing of transmission lines into the vertical port (VP) region. In the context of the DEMO plant, the RF power is generated in an adjacent RF building and transferred to the tokamak building via TL (Fig. 26(a). From the ex-vessel area in the tokamak building, TLs pass through the bioshield and cryostat before bending 90° downward into the VP. The vacuum boundary is indicated by dashed orange lines in Fig. 26a, where vacuum windows should be installed along the TLs, after which they operate under high-vacuum conditions. TLs consist of interconnected segments of customized lengths. Standard industrial components are available in various diameters, bends, and junctions, allowing routing flexibility in the DEMO environment. Fig. 26b provides a more realistic view of the VP space, showing segmented TLs with 90° bends above the VP closure plate. Additional specialized components, such as bellows to accommodate thermal expansion of the vacuum vessel, dogleg bends

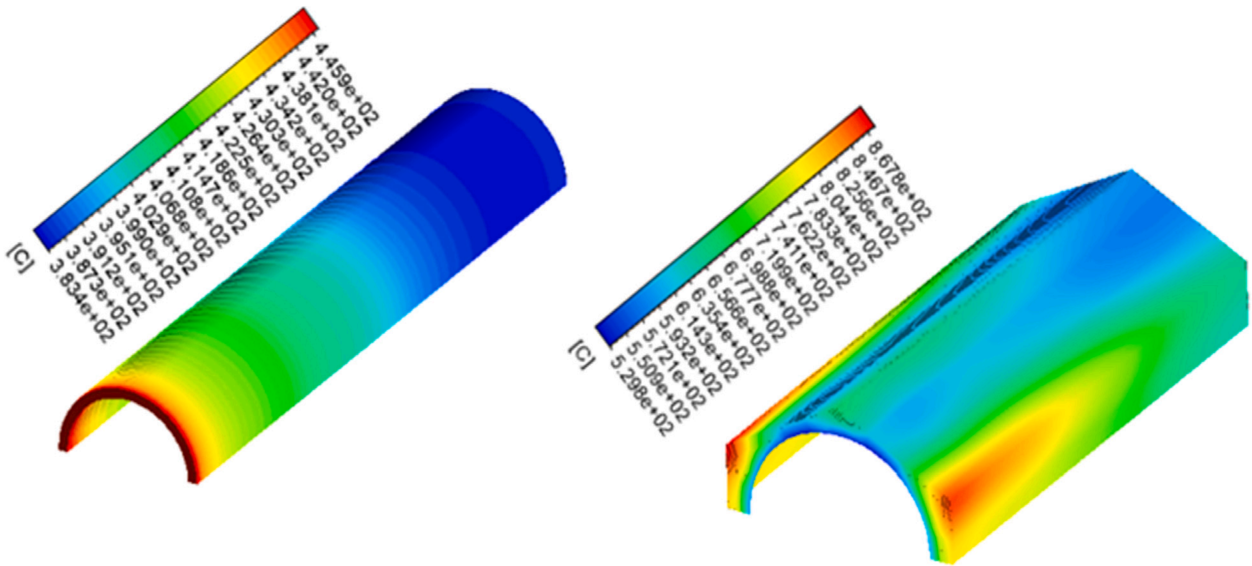

Fig. 23. Temperature distribution in the outer conductor (left) and surrounding neutron-multiplier region (right). The hottest regions are those closest to the plasma side.

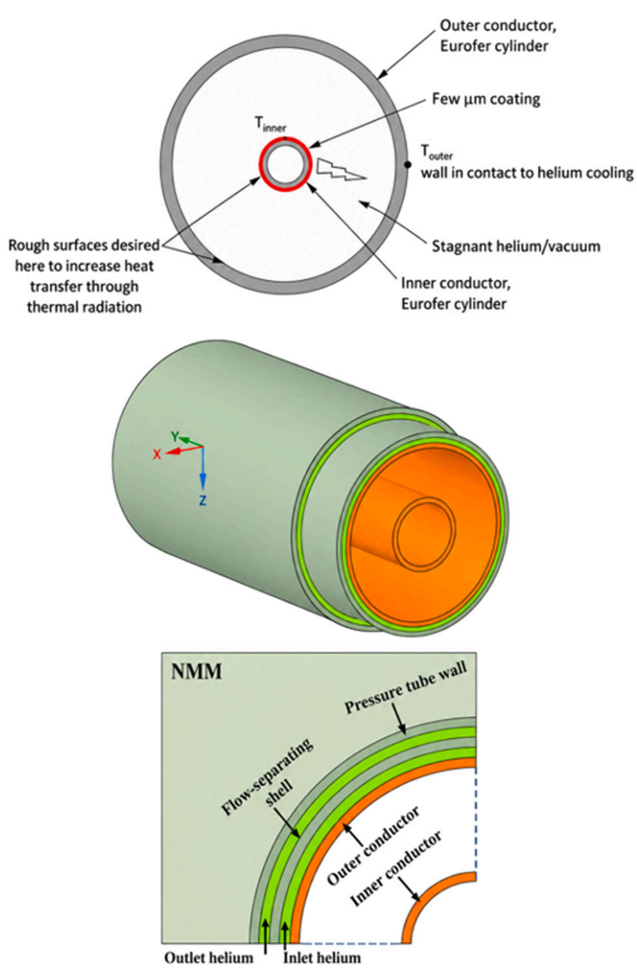

Fig. 24. Radiation-cooling set-up and geometry used for the inner-conductor thermo–hydraulic analysis. A quarter model is used owing to symmetry.

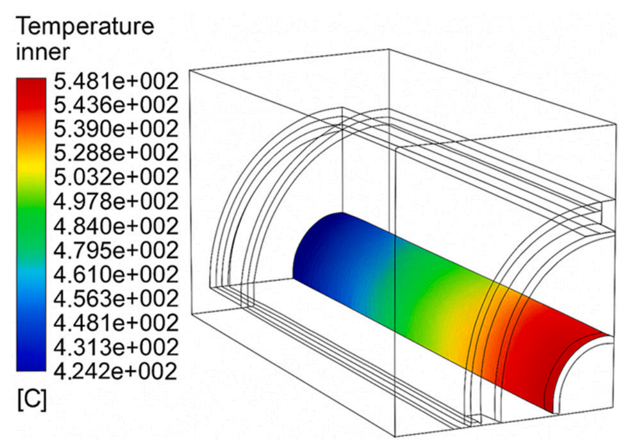

Fig. 25. Temperature distribution on the inner conductor via radiation exchange with the outer conductor for the case of an emissivity of 0.5.

to mitigate neutron streaming, and quick disconnect flanges (Fig. 5) for RH compatibility, may also be required. Fig. 27 shows the VP region that includes the blanket coolant pipes. The current configuration shows that there is sufficient space for both the TLs and the blanket coolant pipes in the vertical port space. TLs interface with the blanket through the chimney (the oval-shaped pocket labeled '4' in Fig. 27), which also provides the grip pocket of the RH manipulator. Importantly, TLs are routed away from this interface, ensuring no obstruction during handling. During maintenance, the TLs are disconnected and removed in coordination with the blanket coolant pipes, after which the blanket segment is lifted.

6. Conclusions

This study presents a preliminary engineering feasibility assessment of the integration of a traveling wave antenna (TWA) in European DEMO, with particular focus on its integration with the breeding blanket system. Although the results do not constitute a final design validation, they provide a basis for further engineering development of

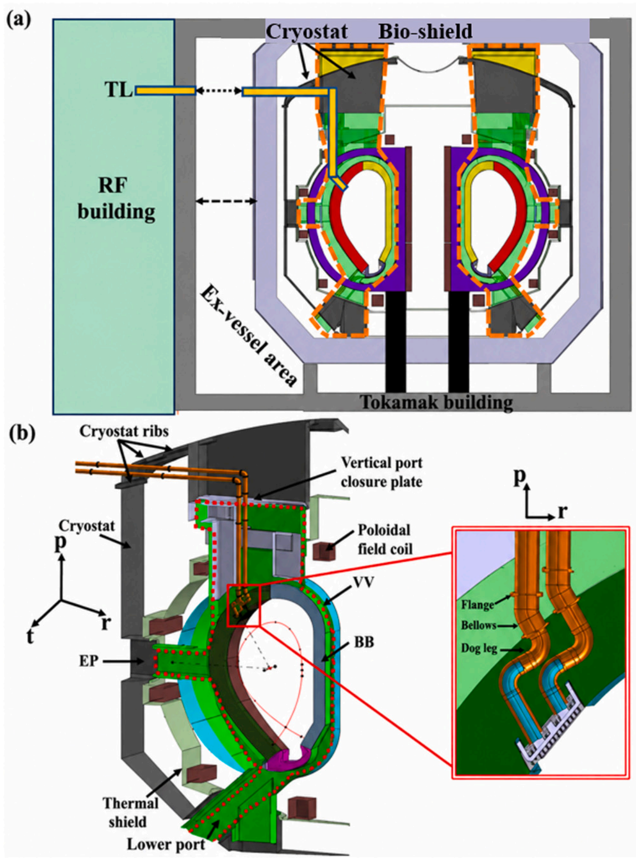

Fig. 26. (a) Two-dimensional view of TL routing in DEMO. (b) Three-dimensional view of TL routing in the vertical-port region, with the main components highlighted. The dashed line indicates the vacuum boundary.

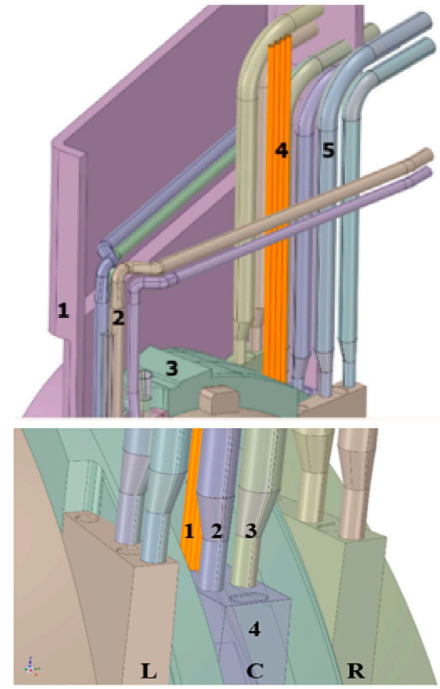

Fig. 27. Top: view into a vertical port: (1) Vacuum Vessel, (2) inboard-blanket coolant pipes, (3) port-plug shield, (4) transmission lines, and (5) outboard-blanket coolant pipes. Bottom: (1) TLs, (2) and (3): blanket coolant pipes, (4) blanket chimney. 'L', 'C', and 'R' refer to Left, Central, and Right blanket segments, respectively in this back-end view.

the TWA concept in DEMO. A simplified tritium breeding assessment, based on a homogeneous material mixture, indicated that under this assumption, the tritium breeding ratio (TBR) remains within acceptable limits. This analysis was intended as a screening-level assessment of the incremental penalty associated with antenna integration, rather than as a high-fidelity blanket qualification exercise. In addition, conditional remote-handling compatibility was demonstrated for the current antenna configuration, while it was also shown that future additions, such as a return-current box behind the antenna, would require a renewed assessment. Thermo–hydraulic analyses of the straps and transmission lines indicate promising performance for the straps and the outer transmission line conductors. At the same time, inner-conductor cooling remains exploratory and strongly dependent on the assumptions adopted. Structural checks of the straps, performed for normal operating loads and monotonic damage modes, indicate compliance with the relevant criteria of RCC-MRx. However, structural integrity under more general loading conditions, including cyclic stresses and transient loads, remains to be demonstrated. The present structural assessment should therefore be regarded as an initial structural viability check rather than a full qualification. The key findings of this preliminary assessment are as follows:

- The tritium breeding ratio is reduced by approximately 2%, while remaining above the required value (> 1.15).
- The strap temperatures remain below 500 °C, and the outer-conductor temperatures of the transmission-line remain below 450 °C, with acceptable pressure drops.
- The structural analysis shows that the straps satisfy the RCC-MRx criteria for monotonic damage modes under operational loads.
- For the configuration considered here, the remote-handling compatibility appears to be preserved, with no collisions identified between transmission lines, coolant pipes, or manipulator interfaces.

The main open points are inner-conductor cooling, the design of the strap-transmission line interface, neutron streaming, and the structural response to transient events such as seismic loads. These issues will be addressed in future work, together with potential design optimizations aimed at further improving thermal performance. Overall, the present results support the TWA as a promising candidate for plasma heating in DEMO and indicate preliminary engineering feasibility, subject to further investigation of the remaining open points.

CRediT authorship contribution statement

Amro Bader: Writing – original draft, Visualization, Validation, Software, Methodology, Investigation, Formal analysis, Data curation, Conceptualization. **Francisco A. Hernández:** Writing – review & editing, Visualization, Validation, Supervision. **Riccardo Ragona:** Writing – review & editing, Visualization, Validation, Conceptualization. **Guangming Zhou:** Writing – review & editing, Validation, Data curation.

Declaration of competing interest

The authors declare the following financial interests/personal relationships which may be considered as potential competing interests: Amro Bader reports financial support was provided by European Consortium for the Development of Fusion Energy. If there are other authors, they declare that they have no known competing financial interests or personal relationships that could have appeared to influence the work reported in this paper.

Acknowledgments

This work has been carried out within the framework of the EUROfusion Consortium and has received funding from the Euratom research and training programme 2014–2018 under grant agreement No 633053. The views and opinions expressed herein do not necessarily reflect those of the European Commission.

References

[1] V. Bobkov, et al., Multi-strap in-port ICRF antenna modelling and development in support of ITER and EU-DEMO, AIP Conf. Proc. 2984 (2023) 060010.
[2] R. Ragona, A. Messiaen, Conceptual study of an ICRH traveling-wave antenna system for low-coupling conditions as expected in DEMO, Nucl. Fusion 56 (2016) 076009.
[3] R. Ragona, A. Messiaen, Study of a distributed ICRF antenna system in DEMO, in: Proc. 22nd Topical Conf. on Radiofrequency Power in Plasmas, RFPPC, 2017.
[4] G. Bosia, Low power density ion cyclotron arrays for fusion reactors, Fusion Eng. Des. 92 (2015) 8–15.
[5] R. Ragona, et al., A travelling wave array system as solution for the ICRF heating of DEMO, Nucl. Fusion 60 (2019) 016027.
[6] R. Ragona, et al., Status of the radiofrequency modelling of the WEST ion cyclotron travelling wave array launcher, Fusion Eng. Des. 218 (2025) 115168.
[7] M. Kwon, et al., Current status of nuclear fusion energy research in Korea, Nucl. Eng. Technol. 41 (4) (2009) 455.
[8] F. Maviglia, et al., Integrated design strategy for EU-DEMO first wall protection from plasma transients, Fusion Eng. Des. 177 (2022) 113067.
[9] R. Ragona, A. Messiaen, Multi-section traveling wave antenna for heating of large machines as DEMO, Fusion Eng. Des. 123 (2017) 232–235.
[10] A. Bader, et al., Integrating a distributed antenna in DEMO: requirements and challenges, Fusion Eng. Des. 123 (2017) 431–434.
[11] U. Fischer, et al., Required, achievable and target TBR for the European DEMO, Fusion Eng. Des. 155 (2020) 111553.
[12] O. Crofts, et al., EU DEMO remote maintenance system development during the pre-concept design phase, Fusion Eng. Des. 179 (2022) 113121.
[13] R. Ragona, personal communication.
[14] F.A. Hernandez, et al., An enhanced, near-term HCPB design as driver blanket for the EU DEMO, Fusion Eng. Des. 146 (2019) 1186–1191.
[15] G. Zhou, et al., Thermal hydraulics activities for consolidating HCPB breeding blanket of the European DEMO, Nucl. Fusion 60 (2020) 096008.
[16] A. Gioè, et al., Exploratory thermal and fluid-dynamic assessment of a pin-based variant of the helium-cooled pebble-bed breeding blanket for the EU-DEMO reactor, Fusion Eng. Des. 218 (2025) 115243.
[17] P. Arena, et al., Design of the WCLL BB in view of the conceptual design phase, Fusion Eng. Des. 218 (2025) 115205.
[18] J.A. Kulesza, et al., MCNP® Code Version 6.3.1 Theory & User Manual, Los Alamos National Laboratory, 2024, LA-UR-24-24602, Rev. 1.
[19] Dassault Systèmes, CATIA, version 5, Dassault Systèmes, Vélizy-Villacoublay, France. Available at: https://www.3ds.com/products/catia.
[20] Inc. Ansys, Ansys SpaceClaim, version 19.2, Ansys, Inc., Canonsburg, PA, USA, Available at: https://www.spaceclaim.com/.
[21] L. Lu, et al., Improved algorithms and advanced features of the CAD to MC conversion tool McCad, Fusion Eng. Des. 89 (9–10) (2014) 1885–1888.
[22] G. Schnabel, et al., FENDL: A library for fusion research and applications, Nucl. Data Sheets 193 (2024) 1–78.
[23] G. Zhou, et al., The European DEMO helium cooled pebble bed breeding blanket: Design status at the conclusion of the pre-concept design phase, Energies 16 (2023) 5377.
[24] P. Pereslavtsev, et al., DEMO tritium breeding performances with different in-vessel components configurations, Fusion Eng. Des. 166 (2021) 112319.
[25] T.R. Barrett, et al., Designs and technologies for plasma-facing wall protection in EU DEMO, Nucl. Fusion 59 (2019) 056019.
[26] G. Zhou, et al., Design study on the new EU DEMO HCPB breeding blanket: Thermal analysis, Prog. Nucl. Energy 98 (2017) 167–176.
[27] C. Bachmann, et al., Initial definition of structural conditions in DEMO, in: Proc. 29th Symp. on Fusion Technology, SOFT 2016, 2016.
[28] Inc. Ansys, Ansys Mechanical, version 19.2, Ansys, Inc., Canonsburg, PA, USA, Available at: https://www.ansys.com/.
[29] M. Garcia, et al., Design and construction rules for mechanical components of high-temperature, experimental and fusion nuclear installations: the RCC-MRx code last edition, Mech. Eng. J. (2020) 7, http://dx.doi.org/10.1299/mej.20-00052.
[30] Y. Chen, F. Arbeiter, Optimization of channel for helium cooled DEMO first wall by application of one-sided V-shape ribs, Fusion Eng. Des. 98–99 (2015) 1442–1447.
[31] J.-M. Noterdaeme, et al., The ASDEX upgrade ICRH antenna, Fusion Eng. Des. 24 (1–2) (1994) 65–74.
[32] G. Zhou, et al., Engineering design of the European DEMO HCPB breeding blanket breeder zone mockup, Appl. Sci. 13 (4) (2023) 2081.
[33] G. Zhou, F. Hernandez, personal communication.
[34] R. Ragona, et al., Overview of the TWA concept from DEMO to the high power mock-up for WEST, AIP Conf. Proc. 2984 (2023) 030014.
[35] R. Ragona, Status of the WEST travelling wave array antenna design and results from the high power mock-up, Nucl. Fusion 62 (2022) 026046.